Probing Oxide Surfaces by Ion Scattering and Recoil Spectroscopy

By

Pim Bram Rossen

A thesis submitted in partial satisfaction of the

requirements for the degree of

Master of Science

in

Engineering- Materials Science and Engineering

in the

Graduate Division

of the

University of California, Berkeley

Committee in charge:

Professor R. Ramesh, Chair
Professor Junqiao Wu
Professor Sayeef Salahuddin

Fall 2011

Voor oma Marie

# ACKNOWLEGDEMENT

# TABLE OF CONTENTS

# 1 INTRODUCTION

## 1.1 Analysis of surface composition and structure

Surfaces are ubiquitous in everyday life as they play an active role in enabling or in being a bottleneck for various technologies. Interactions and reactions in materials, of any scale, are through surfaces and they play a crucial role in micro- and nanotechnology. In integrated circuits the device structures are often built up by depositing different layers of (semiconducting) materials and (etched) surfaces. With the ongoing quest for smaller components the surface to bulk ratio is increasing and their properties and more and more determined by the surface. For heterogeneous catalysts, where reactions occur at the surface, the structure and composition control the effectiveness of the catalyst. In the growth of thin film complex oxides the composition of the topmost atomic layer can be determinant of the presence and magnitudes of characteristic phenomena. The present interest in surface sciences was marked by the Nobel Prize in Chemistry 2007, which was awarded to Gerhard Ertl for his advancements in surface chemistry.

The atomic structure and composition of materials often differ from those of the bulk, in order to reduce surface energy. This difference can feature perpendicular (relaxation) or parallel (reconstruction) atomic displacement, changes in the chemical composition, and the creation of chemical bonds with adsorbed species. To probe the structure and properties of the surface that are different from the bulk analysis techniques are required that are surface sensitive. Since the length scales associated with surface properties are in the order of atomic separation lengths, the analysis techniques are ideally sensitive on a scale down to the topmost atomic layer(s). Many surface analysis techniques have been developed to answer the questions concerning the elemental composition and the atomic structural arrangement of surfaces. These techniques are all based on the methodology of sending in particles and analyze the response after the interaction with the surface. The particles used in these analysis techniques can be electrons, photons or ions.

When using ions to probe surfaces one analyzes the energy and mass of scattered and/or recoiled atoms and ions. The foundation is the interaction of a beam of monoenergetic, mass-selected, collimated ions with a kinetic energy in the low keV range. At the surface, as a result of one or several interactions, some of the primary ions will scatter off the surface and some of the atoms in the top layer of the surface may be recoiled off the target. During the interactions an electronic charge exchange occurs, which results in the creation of neutral, positive and negative charge states. As a result of the quasi-single collision from the primary ion impinging on the surface the scattered and recoiled ions have discrete kinetic energies in the same range as the primary ion prior to the interaction. High enough energy to break atomic bonds and low penetration depth make ion scattering a popular tool for compositional analyses. Additionally, because of a de-Broglie wavelength that is typically less than a hundredth of an angstrom ion scattering and recoil techniques have no detectable interference effects. The atomic

arrangement provides highly anisotropic flux signatures that are used for crystal structure determination. The absence of interference allows for a more straightforward analysis based on classical mechanics. When crystals are the subjected to the incoming primary ion beam the incident atoms are guided and focused spatially by the arrangements of the atomic cores. Due to mass and angular dependence of the interactions at the surface ion scattering is element specific.

## 1.2 Ion scattering

In principle any element in the periodic table can be used to make up the probe beam. In general for ion scattering the incident ion energy of the probe beam determines the types of interaction with the target [1]. In the hyperthermal regime, ranging from 1 to 500 eV, the energy is close to chemical bond energies, electronic excitation and ionization energies. Phonon and electronic excitation, as well as ionization and subplantation are typical effects in this energy range. Secondary ion mass spectroscopy (SIMS) uses the detection of species with hyperthermal energies to determine the (bulk) chemical composition of targets [2]. Using high energy nuclei, >100 keV, proton, alpha, or heavier ions scatter from the nuclei of atoms in the target, or cause x-ray, ion, or neutron emission from interactions. These interactions are employed by Rutherford backscattering spectroscopy (RBS) to probe the long range atomic order and elemental makeup of bulk samples at depths of up to many micrometers [3]. In the intermediate, low energy, region of several keV the chemical bond and electronic energies are much lower than the ion energy and heavy ion beams may be scattered from surface atoms or may cause removal of neutral, ionized, or excited atoms from the surface layer. Historically Low energy ion scattering (LEIS) was one of the less used ion scattering techniques due to a marginal mass resolution, high required beam dose, and quantitation difficulties. However, it was realized that experiments could be performed by pulsing incident ion beams and using time-of-flight (TOF) for the energy analysis of scattered primary particles and recoiled surface atoms [2]. The technique that uses the flight time of scattered and recoiled ions to probe surfaces is called Time of flight ion scattering and recoil spectroscopy (TOF-ISARS).

The general capabilities of TOF-ISARS can be summarized to the following points [4]. The elemental analysis will present every element on the surface of the probed sample. With a sensitivity of < 0.01 monolayer all (contaminating) species, inducing hydrogen, will be detected in a single experiment. The structural analysis offers a simple direct method in real space for determining interatomic distances in surfaces to < 0.1 Å, Surface relaxation and reconstruction as well as adsorption site positions for chemisorbed species have been determined using this technique. Used is a low dose that gives a ratio between the primary ions to surface atoms in the order of $< 10^{-3}$, making this technique relatively nondestructive. It has been demonstrated that this technique can be used to study insulating samples, such as polyester, without observable charging effects even with an insulating method of mounting the sample to its holder [5].

## 1.2.1 THEORETICAL DESCRIPTION AND MODELING OF ATOMIC INTERACTION

The processes involved in ion scattering are too complex to be described by a many body approach, common in solid state theory. In order to achieve sufficient high accuracy it is common practice to regard ion scattering and recoiling events as pairwise interactions. This assumption is validated by the kinetic energies that are much higher than the thermal and binding energies in solids as well as the interaction times which are much shorter than phonon frequencies. For most experimental works a simple kinetic description of collisions has been regarded as sufficient, although theoretical understanding has been extended by addressing the interaction potential and directional effects in ordered solids. In this section I will introduce the primary concepts in each of these areas and their implications, for a more extensive treatment I would like to refer to the textbook written by J.W. Rabalais [6].

### 1.2.1.1 Kinematics

Describing the final states of the particles the kinematic model does not give information on the positions and energies of the particles during the interaction. The model described here is based on the Binary collision approximation (BCA), which regards the trajectories of energetic particles as a series of straight lines corresponding to the asymptotes of the scattering trajectories due to sequential binary collisions [6]. The final energies after the scattering process can therefore be found using only the conservation of energy and momentum. The momentum of the projectile after the interaction is given by the following equation:

$$p_1 = p_0 \frac{\cos\theta \pm \sqrt{\cos^2\theta - (1 - M_2/M_1)(1 + M_2/M_1)}}{1 + M_2/M_1} \tag{1}$$

In this equation the subscript 0 and 1 are given to the primary atom before and after the collision, subscript 2 refers to the target atom, and angle $\theta$ is the difference between in initial and final direction of the primary atom. Expressing the states in terms of kinetic energy is more common rather than momentum, giving a more general expression for both $M_1 < M_2$ and $M_1 > M_2$, where the kinematic factor K gives the relation between the initial and final kinetic energy.

$$E_1 = E_0 \left(\frac{M_1}{(M_1 + M_2)}\right)^2 \left(\cos\theta \pm \sqrt{\left(\frac{M_2}{M_1}\right)^2 - \sin^2\theta}\right)^2 = KE_0 \tag{2}$$

The energy of the recoiled target particle is derived in a similar fashion, presented in the next equation, where T presents the fraction of energy transferred and angle $\phi$ is the difference between the initial direction of the primary atom and the direction of the recoiled atom.

$$E_2 = E_0 \frac{4M_1 M_2}{(M_1 + M_2)^2} \cos^2 \phi = T E_0 \tag{3}$$

The flight time t from the target to the detector, separated by length L, for a particle with kinetic energy E and mass M is given by:

$$E = \frac{ML^2}{2t^2} \tag{4}$$

For the final trajectory it is given by the elastic energy losses related with the interaction between nuclei and momentum transfer.

### 1.2.1.2 Interactions

In order to understand the mechanism of scattering and recoiling at the surface of the target it is necessary to take a closer look at the dynamics of atom interaction. As the distance between two atoms is decreased the electronic clouds start overlapping and a complex interaction of the nuclei and electrons of the two atoms occurs. The interatomic potential is a result of this overlap and interaction. We are interested in the potential as a function of the distance r between the nuclei.

$$V(r) = \frac{C}{r} \varphi(r) \tag{5}$$

The screening function $\varphi(r)$ represents the deviation from a purely coulombic interaction. These approximations generally consist of sums of exponential functions for the dependence on the distance between nuclei, through a quantity referred to a as the universal screening length. Most commonly used is the Ziegler-Biersack-Littmark (ZBL) screening function, which includes coulombic, electronic overlap and exchange contributions in the potential as well as a more realistic charge distribution around the nucleus [7]. In their study detailed calculations of the solid-state interatomic potential of 261 atom pairs were performed and they arrived at the universal screening function:

$$\Phi(r) = 0.1818 \exp\left(-3.2\frac{r}{a}\right) + 0.5099 \exp\left(-0.9423\frac{r}{a}\right)$$
$$+ 0.2802 \exp\left(-0.4029\frac{r}{a}\right) + 0.02817 \exp\left(-0.2016\frac{r}{a}\right) \tag{6}$$

With a screening length $a_{ZBL}$ in terms of the atomic numbers of the two atoms and the first Bohr radius, $a_0 = \hbar^2/me^2$.

$$a_{ZBL} = \frac{0.88534}{Z_1^{0.23} + Z_2^{0.23}} a_0 \tag{7}$$

Note that the ZBL potential for an isolated atom is not defined and therefore this screening function should not be used for calculating the electron distribution of isolated atoms. For the energy range of TOF-ISARS experiments, several keV, this potential

provides a good approximation. Only when lowering the energies down to 30-50 eV more sophisticated models will be required [6]. Another effect of the typical energy range are the small electronic energy losses and these can safely be neglected, both as a source of inelastic energy loss and as a cause for changes in the trajectory.

### 1.2.1.3 Shadowing and blocking cones

The interatomic potential described in the previous paragraph describes the mutual repulsion between the projectiles and target particles. There are two manifestations of this ion-blocking phenomenon that are playing significant roles in ion scattering and recoil experiments, presented in Figure 1. The first is the appearance of regions behind target atoms that are not allowed for penetration by the incident particles, called shadow cones. The second appears when forward scattered or recoiled atoms are directed towards their neighbors, the repulsive effect of the interatomic potential on the trajectory will create a blocking cone.
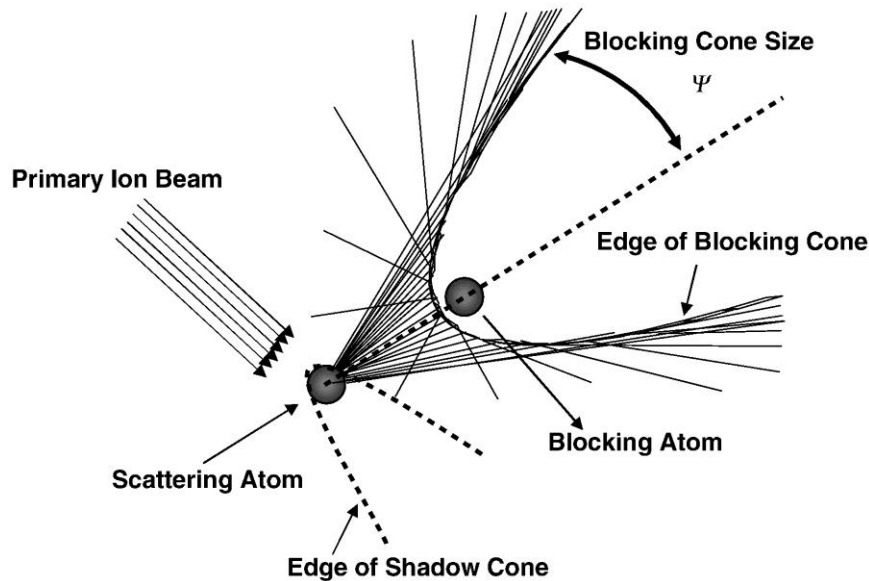


Figure 1. Schematic presentation of shadow and blocking cones [8]

Shadow cones are present when atoms are placed in an incoming parallel flux of particles that are lighter than the target atoms. Within a certain area the scattering angle will be large enough to prevent the incoming particles from penetrating the region immediately behind the atom. Using an observation angle close to 180° and a varying incidence angle of the incident beam the Impact-collision ion scattering spectroscopy (ICISS) or Scattering and recoiling imaging spectrometry (SARIS) techniques can be used to determine interatomic distances between the atoms on the surface of a crystal [9].

Blocking cones are manifested as result of the redistribution of the scattered flux. When the parallel flux of particles is incident on the target, the target atoms act as virtual sources that radiate scattered atoms nearly isotropic for large scattering angles. When the

trajectory of a scattered atom intersects with a second atom in the vicinity of the first atom, the repulsive potential will cause the atom to deflect. The apex of the hyperboloid pattern is located on the first atom and the axis of the blocking cone is centered approximately on the line that connects the two atoms. As suggested by Figure 1 the scattered atoms are focused at the edges of the blocking cone, and do not penetrate into it.

### 1.2.1.4  Effect of ordered structure

Even though interference is not present the scattering of ions by well-ordered solids such as crystals, the collisions experienced by a particle are correlated with to the order existing in the crystal. These correlations can significantly change the trajectory after the interaction on the surface in comparison to the trajectory in the random medium. This effect is strongly dependent the initial direction in regard to the crystalline directions. Sharp spatial anisotropy of the scattered and recoiled ion intensity can be observed when the ion beam is incident at a glancing angle. The two effects that give the azimuthal spectra sharp minima and maxima are surface semichanneling and defocusing of trajectories [10, 11]. The patterns created by these effects are a direct measure of surface periodicity.

Semichannels are formed by three close-packed rows parallel atomic rows, two rows in the first atomic layer serve as the "walls" of the channel and a second atomic layer row which serve as the "base" of the channel. Under certain conditions, when the incident plane of the primary ion is parallel to the channel, these surface semichannels are able to focus ions effectively. Maxima due to the focusing and semichanneling along the principal azimuths occur along the low-index azimuthal directions. However, under off-specular scattering conditions, when the outgoing angle is much bigger than the incident angle, minima rather than maxima in the intensity are observed. These minima are representations of the defocussing effect, occurring at large angles along the principal azimuths. Under these conditions the flux is focused along the forward specular direction, because the first-layer atoms lie within the shadow cones of their neighbors. In this case no small impact parameter (large scattering angle) collisions are possible, limiting large angle scattering and recoiling [11].

### 1.2.2  ION SCATTERING AND RECOIL SPECTROSCOPY EXPERIMENTS

Typically Time of flight ion scattering and recoil spectroscopy (TOF-ISARS) experiments yield plots of the measured intensities of scattered and recoiled particles versus the Time of flight (TOF). These TOF spectra are obtained by using pulses of the primary ion beam and subsequently measuring the flight times of both scattered and recoiled particles. Using the equations from paragraph 1.2.1.1 a mass spectrum can be obtained by converting the TOF's. The following variables are present in TOF-ISARS experiments: (1) the mass and atomic number of the incident primary ion beam; (2) the energy of primary ions; (3) the incident angle ($\alpha$) of the ion beam with respect to the sample surface; (4) the azimuthal angle ($\delta_1$) of the crystal with the incident ion beam; (5) the forward scattering (FS) and recoiling (R) angle ($\theta$) with respect to the incident beam; (6) the exit angle ($\beta$) of the particles that are scattered and recoiled; (7) the kinetic energy related to the scattered and recoiled particles; (8) the azimuthal angle ($\delta_2$) of the crystal

with the outgoing scattered and recoiled ions [6]. The angles are schematically presented in Figure 2. Using these parameters two techniques are designed to explore the surface with TOF-ISARS: Direct recoil spectroscopy (DRS) and Mass spectroscopy or recoiled ions (MSRI). When the spectroscopy experiments are performed as a function of the azimuthal angle, the notation 'angle resolved' (AR) is sometimes added (e.g. AR-MSRI).
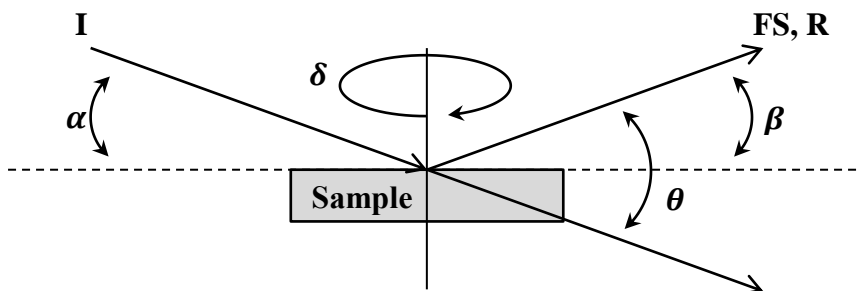


Figure 2. Schematic presentation of the various angles and terms used in TOF-ISARS: Incident angle ($\alpha$) of incident primary ion beam (I), forward scattering (FS) and recoiling (R) angle ($\theta$), exit angle ($\beta$), and azimuthal angle ($\delta$).

### 1.2.2.1 Direct recoil spectroscopy

Direct recoil spectroscopy (DRS) is characterized by a grazing incidence of the primary ion beam and by the detection of scattered primary beam particles and recoiled surface atoms in the forward scattering direction. Typically the incident angle ($\alpha$) and exit angle ($\beta$) are the same (thus equal to $\theta/2$). Surface atoms with a mass higher than the primary beam primarily scatter the primary ions with different kinetic energy losses, allowing the determination of structure and composition by comparing the relative intensity as a function of flight time. Surface atoms with masses smaller than the primary ions are recoiled in the forward scattering direction. Using a suitable primary ion beam surface atoms such as oxygen, carbon, and hydrogen are well resolved [2]. In fact, DRS is one of relatively few surface analytical methods to have good sensitivity for hydrogen and its isotopes [12].

### 1.2.2.2 Mass spectroscopy of recoiled ions

The kinetic energies derived from the equations in paragraph 1.2.1.1 are only valid for an ideal binary collision. In case of multiple collisions each mass has a kinetic energy spread, and not a unique single value, as a result of the loss of energy. The energy spread results in the broadening features towards longer flight times. For this reason mass resolution while using DRS is limited. By using a reflectron time refocusing analyzer, or simply reflectron, (see paragraph 2.1.2.1 for a full description of the mechanism and operation) the flight times for ions with the same mass are homogenized, compensating the spread in kinetic energy of the recoiled ions. The use of a reflectron to improve the resolution of direct recoil spectra is referred to as Mass spectroscopy of recoiled ions

(MSRI) [5]. MSRI has both isotopic resolution for the entire mass range and a sensitivity better than parts per million (ppm) [4]. Because the MSRI technique can only detect ions, with either a positive or negative charge, anisotropic neutralization makes a quantitative interpretation problematic [5]. This marks a long-standing problem in ion-based mass spectrometry affecting both compositional and structural studies [13].

### 1.2.2.3   Other ion spectroscopies

The broad term Ion scattering spectroscopy (ISS) is in principle an overarching term for the various forms of scattering techniques, but in practice it is often used in reference to techniques employing large scattering angles, such as back scattering (BS) spectroscopy. This technique has mainly been employed in the analysis atomic configurations and distances through shadow and blocking cones. Suffering from the same drawbacks as DRS, ISS has a low mass resolution. On a first glance MSRI seems similar to the more commonly used Secondary ion mass spectroscopy (SIMS), yet there are significant differences [14]. The geometries are fundamentally different for MSRI and SIMS. The geometry for MSRI uses a grazing angle for the incident ion beam as well as the detector emphasizing single collision ejection events. In the SIMS process the incident ion beam and detector are perpendicular to the surface, providing the typical multiple collision cascade mechanism. The kinetic energy of recoiled ions by only a single collision is much higher than that of the particles ejected by the collision cascade process. By the time that there is enough normally directed momentum from the cascade for a surface atom to be ejected from the surface, the kinetic energy has typically been degraded to only a few eV, compared to the keV range for MSRI ions. The difference in kinetic energy directly results in a low neutralization probability for MSRI, with ion fractions in the range 10-40%, while the low velocity of the SIMS ions results in very efficient neutralization of the sputtered atoms, with ion fractions in the range $10^{-2}$ to $10^{-4}$. Although this makes MSRI much less subject to the so called "matrix effect", which results in the variation of several orders of magnitude in ion yields for SIMS, it is not totally absent. With a reference sample it is possible to determine the chemical phase of a surface simply by comparing the positive and negative MSRI ion signal ratios.

### 1.2.2.4   Simulations

As discussed previously, when the kinetic energies are much larger than the binding energies in the crystal lattice, the Binary collision approximation (BCA) in classical mechanics provides a good description of the phenomena resulting from particle collisions. Computational programs for simulating ion-solid interactions have been used for a long time [15], and these elementary programs have provided a wealth of information about the collision phenomena. An overview of these programs is given in the review on ions scattering by Niehus et al. (1993) [16]. A limiting factor has been the large amounts of computer time required. In order to operate efficiently on small personal computers Bykov et al. [17] developed a new classical ion trajectory simulation program, called Scattering and recoiling imaging code (SARIC), which provides data directly related to the information obtained from their TOF measurements for surface structure determinations. The SARlC code describes particle interactions in the linear cascade approximation, meaning that there is not interaction between different particles involved

in the same cascade or between particles from two sequential cascades. When the ion beam fluence is less than $\sim 10^{10}\ ions/s\ cm^2$ and the kinetic energy of the primary ions is in the range $1 - 5$ keV, these assumptions are valid. The primary operation of the SARIC program is the procedure that follows particles, either primary ions or recoiled atoms, moving within the boundaries of the target. The particles are followed as long as their energies are greater than the minimum detection energy and they are within the target boundaries. When no longer satisfying these criteria, the particles are dropped from consideration and a new primary ion is started. Either the Ziegler-Biersack-Littmark (ZBL) or the Moliere screening function is used for the calculations to simulate the three-dimensional motion of atomic particles. In support of TOF-ISARS experiments, the energy and time-of-flight distributions of scattered and recoiled ions, incident angle scans, and azimuthal angle scans can be calculated by the SARIC program [17].

## 1.3  Control and understanding of surfaces and interfaces

In the past two decades TOF-ISARS techniques have been employed in studies investigating the structure, composition and chemistry of surfaces of both crystalline films and substrates. Given the complexity of TOF-ISARS, it is instructive to assess the methods and results of a selection of these studies. First the analyses of surface structures and termination will be addressed followed by compositional analyses and contaminants.

### 1.3.1  SURFACE STRUCTURE AND TERMINATION

To determine which of the elements of the bulk material make up the topmost layer of the sample and the crystal structure of this layer DRS and (AR-)MSRI have been employed for $TiO_2$, $CeO_2$, $BaBiO_3$ and $SrTiO_3$ [18,19,13,21]. Using a small angle of incidence these authors have studied the azimuthal angular dependence of the individual elements.

The microfaceted (1x4) surface reconstructions on the surface of $TiO_2$ (001) were reported after observation by Low energy electron diffraction (LEED) and analysis by experimental and simulated AR-MSRI [18]. An incident angle $\alpha$ of 10° was used and the MSRI detector was located at $\theta = 70°$. The azimuthal spectra for $Ti^+$ and $O^+$ ions have minima in intensity at 0° and 90° and very distinctive features in the range 15 - 75°. The $O^+$ spectrum has broad peaks at 17° and 73°, and the $Ti^+$ spectrum shows have four peaks at 20°, 36°, 54°, and 70°. Out of the simulated reconstruction models only the microfaceted model (MFM) were in agreement to experiment, reproducing the characteristic peaks for both $Ti^+$ and $O^+$, providing evidence for (103) and ($\bar{1}$03) facets.

Using a 5 keV $Ar^+$ beam ($\alpha = 20°$), AR-MSRI ($\theta = 60°$) and DRS ($\theta = 24°$) the surface of $CeO_2$ (001) samples, grown Molecular beam epitaxy (MBE) on a $SrTiO_3$ (001) substrates, was determined to be terminated with 0.5 monolayers of oxygen [19]. From DRS experiments it was expected that the surface is terminated by an oxygen layer. Comparing the $Ce^+$ spectrum from the AR-MSRI to that of SARIC simulations of full layer terminations of both cerium and oxygen and 0.5 monolayer termination of oxygen, it was found that the latter provided the best fit. This result is consistent with a predicted

model based on reducing the surface dipole moment. Using the same setup, surfaces of $Y_2O_3$-stabilized $ZrO_2$ (YSZ), (100) and (110), were analyzed [20]. The MSRI spectra for both orientations are similar, except the presence of $Mg^+$ for the (100) sample and $Cs^+$ in the (110) sample. The ratio between $Zr^+$ and $O^+$ is nearly identical for the two orientations. The influence of annealing was observed by DRS, in the (by sputtering) cleaned samples a substantial $Ar_S(Zr/Y)$ peak is present and after annealing this scattering peak is greatly reduced (100) or complete eliminated (110), leaving only the multiple scattering (MS) peak present. The authors suggested that the surface concentration is dominated by oxygen after annealing, and recommended AR and variable incidence angle studies for further investigation.

The termination of the perovskite $BaBiO_3$, grown by MBE on $SrTiO_3$ (001) substrates, was investigated by using DRS ($\alpha = 15°$ and $\theta = 37°$) and MSRI ($\theta = 37°$) [13]. At $\theta = 37°$, the peak for potassium scattered of bismuth $K_S(Bi)$ is independent of azimuthal angle between 3.5° and 10.5°, whereas the peak for potassium scattered of barium $K_S(Ba)$ drops rapidly in intensity. Comparing the $Bi^+$ signal from AR-DRS from 0 to 45 degrees, with characteristic peaks at 21° and 33°, to SARIC simulations for BiO and BaO terminations shows a match between the experiment and BiO simulation.

The surface of $SrTiO_3$ substrates was investigated using a 3 keV $Ar^+$ beam ($\alpha = 12°$) and DRS ($\theta = 45°$) [21]. The azimuthal dependence of the signal intensity of recoiled oxygen atoms $O_R$ and scattering by strontium atoms $Ar_S(Sr)$ was monitored and compared to SARIC simulations. Both the $O_R$ and $Ar_S(Sr)$ spectra exhibit a 90° periodicity with deep minima at 0°, 90°, and 180°, which are accounted for by shadowing and blocking are encountered along these high symmetry directions. When the oxygen atoms in the top layer were elevated 0.1Å above the surface plane the best agreement was found between the experimental and simulated δ scans for both the oxygen and strontium data.

### 1.3.2 SURFACE SPECIES, INTERMIXING AND GROWTH

Using MSRI and DRS the diffusion between various layers ($SrBi_2Ta_2O_9$, Pt, Ti, and $SiO_2$ onto Si) during growth and the adsorption of hydrocarbons on Si and $Al_2O_3$ substrates were studied [12,14,22,23,24]. A higher incidence angle was used to direct the shadow cones downward, increasing the sensitivity while reducing the angular dependence.

The surface composition before and during growth of layered perovskite $SrBi_2Ta_2O_9$ (SBT) onto a bottom electrode structure of Pt (150 nm) / Ti (50 nm) / $SiO_2$ (200 nm) / Si were studied by TOF-ISARS [12, 14]. The parameters reported are the use of a 10 keV $Ar^+$ ion beam and the positions of the detectors, DRS ($\theta = 25°$) and MSRI ($\theta = 60°$). For the electrode structure high $H^+$ and $C^+$ MSRI signals are present at any temperature and above 450°C $Ti^+$ and $Si^+$ peaks increase dramatically, indicating segregated Ti and Si on the surface. During deposition of SBT the $Pt^+$ peak disappears, and the $Ti^+$ and $Si^+$ peaks diminish in intensity and signals disappear entirely upon cooling down. Another cooling effect is the increasing bismuth signal until at 400°C, the

Ta and Bi signals are equal in magnitude and stay the same. The authors relate this behavior to a competition between Ti and Si on one hand and Bi on the other for the available oxygen. Using the same methodology the growth of barium strontium titanate (BST) films on silicon was studied [22]. The $Si^+$ signal decreases more rapidly on an oxidized silicon substrate, indicating a smaller area of intermixing of the film and substrate.

The annealing of Si and $Al_2O_3$ substrates was monitored by TOF-ISARS [23]. Using 5 keV $Ne^+$ ion beam ($\alpha = 22.5°$) and DRS and MSRI ($\theta = 45°$) temperature dependent experiments were performed. For $Al_2O_3$ $H^+$ and $C^+$ peaks remained present while heating up to 600°C, indicating desorption at this temperature, and the $O^+$ signal increases until 860°C and then decreases. For the Si substrate a similar trend was seen for the $H^+$ and $C^+$ peaks, while the $O^+$ signal increases until 760°C after which it drops. A similar study shows that for germanium surfaces the critical temperature for hydrocarbons is approximately 470°C [24].

## 1.4 Application of TOF-ISARS to oxides

In oxides many interesting and diverse properties have been discovered, such as superconductivity, magnetism, and ferroelectricity, making them an interesting class of materials [25,26,27]. Perovskite oxides are commonly used in the formation of strained heteroepitaxial structures of high complexity and grown with atomic precision, which is facilitated by their oxygen backbone structure [28]. New or enhanced functionality foreign to the parent compounds has been shown in individual interfaces as well as repeated multilayers, or superlattices [29,30,31,32]. The conducting interface between the two wide-bandgap insulators $SrTiO_3$ and $LaAlO_3$ has received significant amounts of attention and is an example of functionality determined at an atomic level [29]. Not only have studies investigated the origin of this conductance, device architecture and functionality has been explored as well [33,34]. For the level of control that is required to create these heterostructures it is essential to start with well-defined, crystalline substrates, and with single-terminated atomic planes, as well as a full understanding of the composition and structure of the topmost atomic layer.

Extending this line of thought, during the growth process of superlattices there are many topmost layers that form the base for the next layer. As discussed in the previous paragraph TOF-ISARS is a very suitable technique to verify the termination of the topmost layer and it would be beneficial to extend its application and the application of the newer developed time refocused MSRI to a wider range of perovskite oxides. Using these techniques in-site, the development of crystal structure, composition and contamination can be closely monitored. The research presented in this thesis is designed to investigate oxide surfaces across substrates and grown films, in order to achieve both a higher control over the topmost layers in heterostructures and additional insight into the process element transfer and crystal growth.

# 2   METHODOLOGY

In this chapter the techniques and procedures are presented as they are applied in this study. The physical experimental setup is described first, consisting of the vacuum chamber for Pulsed laser deposition (PLD) with the Time of flight ion scattering and recoil spectroscopy (TOF-ISARS) instrumentation attached. Subsequently the preparation and measurement procedures are described. The last section elaborates on the analyses of the generated data, including the processing of the raw data as well as the interpretation and post processing of measurement series.

## 2.1   Experimental setup

### 2.1.1   VACUUM SYSTEM OVERVIEW

The setup used in this research combines instrumentation for both growth and analysis aspects. The vacuum is created by a two stage pumping combination of rotary vane pumps and Turbo molecular pumps (TMP). The electron gun, the ion gun and the reflectron detector are all differentially pumped by separate TMPs. The growth of thin films is performed by PLD monitored by the Reflection high energy electron diffraction (RHEED), designed by Neocera, Inc. The used RHEED system is the kSA 400 designed by k-Space Associates, Inc. This system consists of an electron gun by STAIB, a P43 phosphor screen, a K200D CCD camera and the analytical RHEED software package. The samples are mounted on a Neocera 2" flat plate heater. At deposition temperatures, 700 °C and up, the base pressure in the chamber is $\sim 10^{-6}$ Torr, and at room temperature the base pressure is $< 10^{-7}$ Torr. Using a SRS RGA 300 it was determined the residual background gas is mainly $H_2O$, with traces of hydrocarbons (mostly 2-isopropanol) and air. The heater is loaded through a load lock to preserve the high vacuum of the central chamber.

### 2.1.2   TOF-ISARS COMPONENTS

The TOF-ISARS system was designed and built by Ionwerks. Inc, and consists of an alkali ion gun and optics, a reflectron detector at $\theta = 60°$ and a regular microchannel plate (MCP) detector at $\theta = 25°$. The position of these components is fixed and cannot be changed between or during experiments. A schematic of the TOF-ISARS components inside the vacuum system is presented in Figure 3. A complete schematic of the electronics and mechanical hardware that make up the TOF-ISARS systems is included in appendix 7.1.
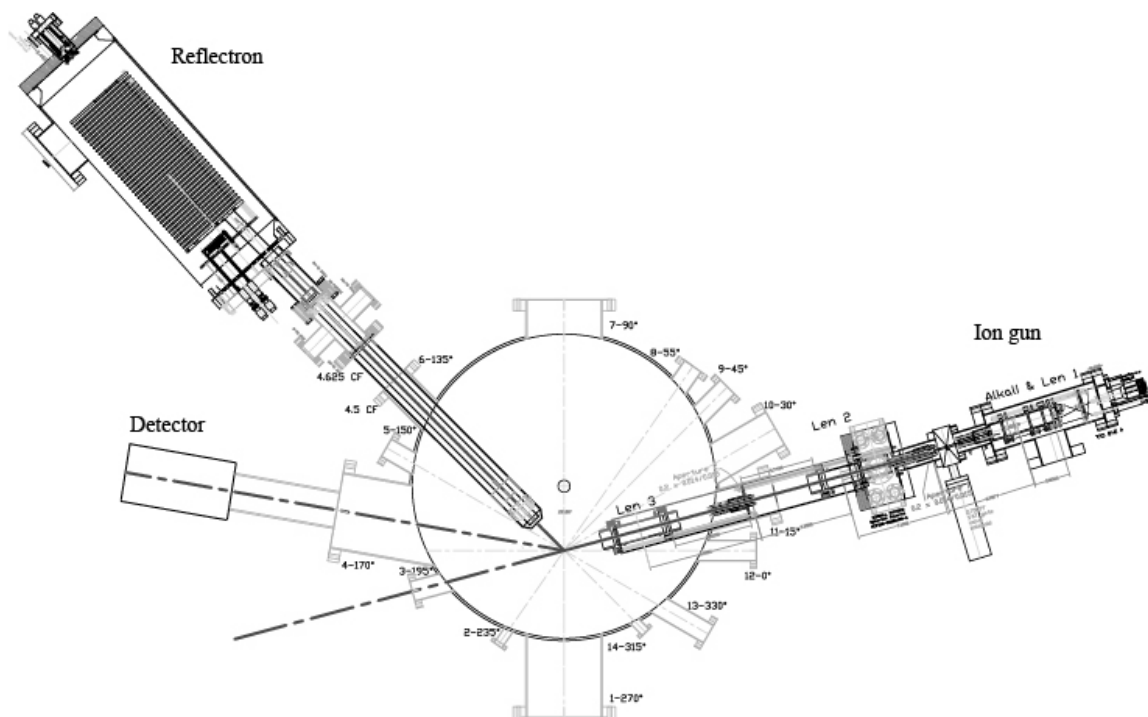
Figure 3. Graphic presentation of TOF-ISARS elements as constructed on the vacuum system (not that orientations, distances and angles may not be accurate). Pictured are the ion gun, the reflectron MSRI detector ($\theta = 60°$) and a scattering and recoil detector ($\theta = 25°$). Not shown are the pulsed laser deposition components (laser beam, heater, target carrousel and RHEED system). Picture courtesy Ionwerks Inc, Houston.

### 2.1.2.1 Alkali ion gun

The alkali ion gun is composed of a source, with beam energy of 10 keV, three focus lenses, three deflection units and 2 slits, as presented schematically in Figure 4. This configuration is designed to give a minimal energy spread. A 2° bend is included through which neutrals are filtered out. The $^{39}K^+$ ion beam is generated by alkali ion source from Heat Wave Labs, Inc (Model 101139-03). To increase the filament lifetime, to avoid loss in ion flux and to reduce the energy spread the ion gun is differentially pumped and operates at a base pressure of 8 x $10^{-9}$ Torr.
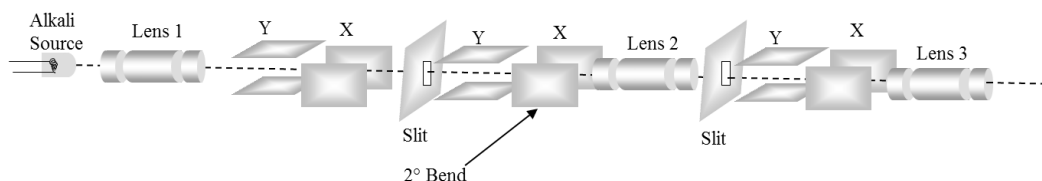


Figure 4. The components of the ion gun and their sequence are presented graphically. The deflection units are represented by sets of parallel plates with the notation X and Y. The 2° bend is located in the second deflection unit, after the beam has passed through the first lens, deflection unit and slit. After the bend there is another lens, a deflection unit and a second slit, behind which there is one more lens.

13

### 2.1.2.2   Microchannel Plate detector

For the TOF measurements microchannel plate (MCP) detectors are used. MCP detectors are arrays of channel electron multipliers (CEM) [6]. CEMs are small tubes over which a field is applied by electrodes on the front and back end. When a charged or fast neutral particle strikes the inside of the tube it causes the ejection of a secondary electron, this electron is then accelerated in the tube and will strike the walls again causing the ejection of more secondary electrons, creating an avalanche of electrons. An anode, collecting the electron pulses, is positioned at the output side of the MCP. Typically MCPs have arrays of 10 μm pores with a wall thickness of 1 μm.

### 2.1.2.3   MSRI Reflectron analyzer

For enhanced energy resolution a reflectron analyzer is used, which is designed so that all ions of a given mass arrive at the detector simultaneously. The reflectron is made up of an extractor aperture, a float tube, the reflectron and two MCP detectors, as presented in Figure 5.
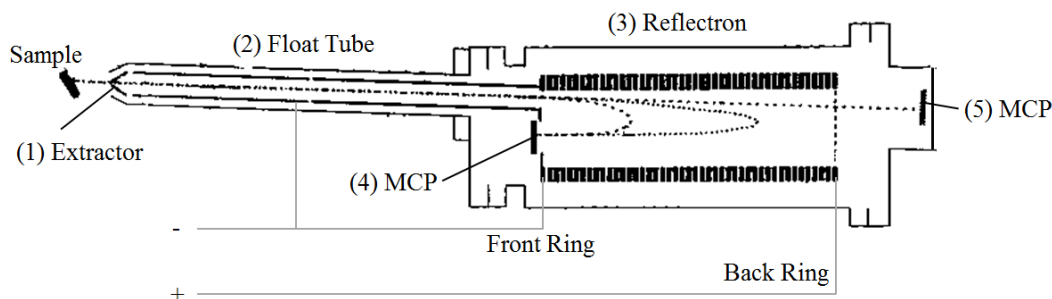


Figure 5. The components and geometry of the reflectron analyzer presented schematically. Five components are numbered: (1) the extractor aperture, (2) the high voltage float tube, (3) the gridless reflectron, (4) the MCP ion detector and (5) the line-of-sight (LOS) MCP neutral detector.

The scattered and recoiled ions enter the reflectron analyzer through an extractor aperture of approximately 1 mm. This aperture, employed to prevent reduction of the signal, allows differential pumping of the analyzer and provides a pressure step of one order of magnitude. A high voltage float potential of -1.15 kV is used to provide a field free drift region from the extraction aperture to the front ring of the reflectron analyzer, which is set to the same potential. The reflectron consists of a vacuum chamber in which an array of potential rings is placed. The voltage of the rings in front of the back ring is set via 1 MΩ resistors connecting successive. This multi ring reflectron setup gives the time refocusing of ion trajectories. The back ring potential is +2.962 kV. In order to properly terminate the field a grid is placed behind the back ring. This high voltage float potential reduces the TOF and decreases the relative kinetic energy spread, increasing resolution of the reflectron. The trajectories of neutral particles are not affected by the created electric fields and these species are collected by the line-of-sight MPC detector.

### 2.1.3 DATA ACQUISITION SOFTWARE

The Microsoft Windows software package Chart Recorder by Ionwerks, Inc is used to acquire TOF data and to subsequently display and export the data on a PC. The data from all three MCP detectors (Channel 1: MSRI, Channel 2: DRS, Channel 3: LOS) are processed simultaneously. The software records the data in a histogram format, with time intervals of 25 ns. For the MSRI data on Channel 1 the software has a calibration option. Based on the allocation of masses to two peaks (oxygen and potassium) the program calculates the masses corresponding to all other TOFs.

### 2.1.4 EXPERIMENTAL LIMITS AND LIMITATIONS

Every system and technique has its limitations and it is important to identify these for both the design or experiments and interpretation of results. The primary ion beam in this system is fixed to 10 keV $K^+$ ions. While higher mass and kinetic energy of the primary ions may give a higher resolution for recoiled ions, especially for high masses, it also results in higher energies of MS particles and approaches the limits of the BCA and application of the SARIC software. Potassium was chosen as the primary ion source for the low neutralization in alkali metals.

In the current configuration the reflectron analyzer has only been employed to detect positive ions. The ratio between positive, negative and neutral species is not only different for every element, but may also be different for the same element in different materials or chemical phases [2]. For this reason one cannot use the absolute values of either (relative) intensities or ratios between (relative) intensities to make a comparison between materials composed of different elements, without knowing the fraction that the positive ions represent of every element in each of these materials. In a previous study, comparing azimuth dependent spectra from the reflectron with and without bias, it was found that the two angular dependencies are essentially identical and that anisotropic neutralization effects (i.e. the change of ion fraction as a function of azimuthal angle) thus are not important [13].

Pressure steps of several orders of magnitude through the extraction aperture have been reported for in-situ use of TOF-ISARS [5, 14]. The experimental setup used in this study has insufficient differential pumping power to provide a pressure $\sim 10^{-6}$ Torr in the reflectron detector and ion gun assemblies, while the chamber is at a pressure used during deposition ($10^{-3} - 10^{-1}$ Torr). An alternative solution could have been to rapidly reduce the background pressure during or after the deposition, while at high temperature. However, $SrTiO_3$ substrates can be reduced rapidly through the creation of oxygen vacancies when exposed to high vacuum at high temperature, causing severe changes to the surface composition and structure [35,36]. For these reasons no in-situ and high temperature studies have been included in this study.

## 2.2   Experimental procedures

The measurement procedures can be divided in the activities prior to, during and after the TOF-ISARS experiments. All samples were subjected to a 5-minute cleaning step for both acetone and 2-isopropanol in an ultrasonic bath. Samples that are straight from the manufacturer (i.e. no surface treatment processes have been applied yet), the so-called 'as received', were cleaned with Trichloroethylene (TCE) before the other solvents. Between after step the samples are blown dry using pressurized dry nitrogen. The sample was then attached onto the polished heater using silver paste, which was hardened by putting the heater on a heating plate set to 100 °C for 10 minutes. Before loading the heater with the sample in the load lock it was blown clean once more with pressurized dry nitrogen. When vacuum in the load lock reached 1 x $10^{-5}$ Torr the heater was mounted on the stage in the main vacuum chamber and moved into position.

If the experiment was designed to analyze a grown film the substrate is heater up to a deposition temperature (850 °C for $SrTiO_3$) in 5.0 x $10^{-2}$ Torr $O_2$ at a rate of 20 °/min. At the growth temperature, but before the growth, the sample was aligned to the (100) direction for the RHEED of the substrate and the target was pre-ablated for 2 minutes at 10 Hz. The film is then grown using 20 ns pulses from a KrF excimer laser (248 nm) using a fluency of 1.5 J/cm$^2$ and a spot size of 7 mm$^2$. The heater is then cooled down to 150 °C at a rate of 10 °/min. If the substrate is to be analyzed the sample is heated up 600 °C at a rate of 20 °/min, after a short anneal of 10 minutes the sample is cooled down to 150 °C at a rate of 10 °/min. It is important to bring the sample to high temperature to clean the hydrocarbons of the surface.

The ion gun is started by slowly increasing the current through the alkali source. The current is increased by steps of 0.05 mA with 30 s intervals, to an operation current of 1.7 mA. To observe a minimum of 30 minutes heat up time of the ion source this procedure is usually carried out during the cooling down. After cooling down the oxygen flow is stopped and the chamber is pumped down to base pressure. The electronics are then switched on and are checked for the correct values. When all checks are completed the high voltage control software and the Chart Recorder are started on the PC. The gate valve between the ion gun and the main chamber is then opened and the sample is aligned so that the MSRI counts/s is maximized.

After alignment the measurement series is carried out, while keeping the sample temperature at 150 °C. Typically, AR-MSRI scans are done from approximately -135° to 75° from the (100) direction with increments of 5° and an angle of incidence of 15°. Due to the design of the heater stage the rotation along the azimuth is limited to this range of 210°. Every individual mass spectrum was captured over approximately 2 minutes, collecting at least 10 000 recoiled ions with the MSRI detector. For verification purposes a measurement at -5° was done before and after the complete series. Differences between these scans could indicate changes in the flux of the ion beam, damage to the surface or adsorption of contaminating species. The total time of irradiation of the ion beam on the sample is 2 to 3 hours.

## 2.3   Analysis

The data is extracted from the files generated by the Chart Recorder program using a Matlab script (using MATLAB R2010B) which is included in appendix 7.2. The data exported by the Chart Recorder for MSRI is calibrated to mass (AMU units) and has a resolution of 0.1 AMU. Thus, individual elements are easily identified. The data for DRS is still a function of TOF and as a result of the system's design the data analysis is less straightforward. Examples of the data exported by Chart Recorder are presented in Figure 6. The data is then plotted and analyzed with OriginPro (version 8.5.1).
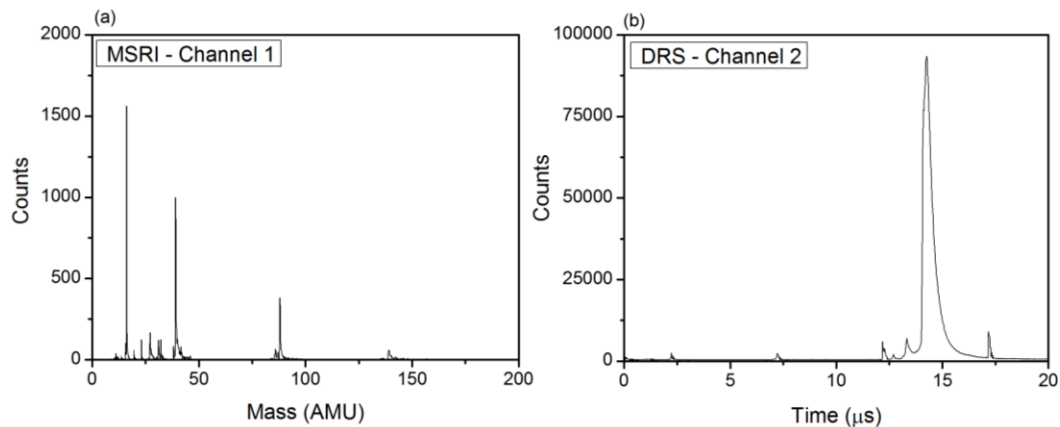


Figure 6. The raw exported MSRI (a) and DRS (b) data from Chart Recorder for a LaSrAlO$_3$ substrate along the (110) direction is presented. Note that the DRS data also features four artifact peaks with a spacing of 5.000 μs starting at 2.225 μs.

### 2.3.1   MSRI DATA ANALYSIS

For the MSRI data on Channel 1 the script integrates the peaks for allocated elements, normalizes the results and exports the data as a function of azimuthal angle. The range for integration is defined by the naturally occurring isotopes of the element in question and the shape of the peak, as present in the data. For elements with a low mass the peaks are sharp and approach the noise level close to the mass of the lightest and heaviest isotopes (<1 AMU). Elements with higher masses have a wider spread and at the base of the peak the measured mass can be separated from the lightest and heaviest isotope masses by 2-5 AMU on each side. The integration limits are set at the points where the measured peak signal approaches the noise level.

The Chart Recorder program is operated by hand and not every histogram was captured for exactly two minutes. To account for deviations in exposure time the integrated peaks are divided by the timestamp included in the data file. The filament is turned on well before the measurement to allow for the flux to stabilize. The recoiled K$^+$ signal is the closest to a measure for the primary ion beam flux impinging on the sample surface. An overall increase in the recoiled K$^+$ signal is present in every measurement

series. The magnitudes of the $K^+$ intensity changes vary wildly between 10% and 100%. The relative intensity varies greatly between experiments (up to a factor 6). Apart from the time the filament current has been on, other factors such as alignment and background pressure may be playing a role. When there is little increase over time the $K^+$ peak shows some angular dependence, with minima along the low index crystalline directions (100) and (010). To use this signal as a method of normalization means that not only information about the angular dependence of the $K^+$ recoil is lost, but also that the angular dependence of the other elements is distorted. Apart from the suggested variation in flux over time there is a difference in intensity between experiments. The comparison between elements of several samples is an argument in favor of normalization by the $K^+$ signal. The extracted data, normalized to time as well as $K^+$, is exported as a table with the azimuthal angle in the first column. A small drift in the sample manipulator is compensated for by manually adjusting the angles so that the minima line up with the crystalline directions.

### 2.3.2 DRS DATA ANALYSIS

There are two types of data features present in the DRS spectra. The strong peak between 14 and 15 μs, with a tail extending towards 17 μs, is the signal from the primary ions scattered off the surface. Small differences in the TOF of potassium particles are caused by the differences in the scattering rate off different surface elements. Each of these peak intensities has a different azimuthal dependency. The small peaks with lower TOFs are the recoiled elements with masses lower than that of potassium. The signals from recoiled elements with higher masses are obscured by the potassium scattering peak. These DRS measurements suffer from the same normalization challenge regarding the variations in flux of the primary ion beam over time and between samples. When integrating over the scattered potassium peak the same observation is made as with the MSRI $K^+$ signal. There is, on average, an increase over time and a variation between samples. The presence of an azimuthal dependence of the integrated scattering signal is clear as well. In order to extract meaningful azimuthal spectra from the individual recoil peak intensity and scattered intensities, there is little choice but to use the integrated intensity as means for normalization. The extracted data is exported in table format with the same azimuthal angles in the first column as the MSRI data.

### 2.3.3 SIMULATIONS

SARIC software has been employed to simulate the angular dependence of recoiled elements. For these simulations the SARIC software was configured following the reports of Gozar et al.[13], Bykov et al. [17] and Van der Heide et al. (2001) [21]. A minimum of 4 unit cell layers was used for the target for the simulations and vibrational amplitude of 0.1 Å. The SARIC software only uses neutral species, resulting in meaningless values for the ratios between different elements, since the ion fractions are different between elements. Since only the shape of the spectra can be used in the analysis it can be normalized and given an offset to fit the experiment. A limitation to keep in mind is the reported validity up to 5 keV of the primary ion beam. The higher energy used in this study is expected to have to most severe effect when collision cascades are prominent. In this case the increased numbers of ejected species are likely to

interact with each other, violating the linear cascade approximation. At the grazing incident angles employed in this study, binary interactions are expected to be the dominant and different members of the same cascade and between cascades are not expected to interact. Therefore, despite operating outside the range for which validity has been reported, the simulations are expected to be representative for the experiments.

# 3 RESULTS

## 3.1 Singly terminated substrates

Substrate surfaces that are smooth and well-defined are of great importance for the fundamental understanding of complex oxide heterostructures and the epitaxial growth involved in this research. For the growth of heterostructures that are built up of perovskite building blocks it is required that the starting surface is 'singly terminated', it has only one type of cation present at the topmost layer. Until recently, with the reports about singly terminated (110) oriented rare-earth scandates and $La_{0.18}Sr_{0.82}Al_{0.59}Ta_{0.41}O_3$ (LSAT) [37,38], perovskite strontium titanate ($SrTiO_3$) with (001) orientation were the only available perovskite substrates of which the termination could be controlled [39]. In this section the results are discussed of three projects that are extending the availability of atomically controlled substrates.

### 3.1.1 (001), (110) AND (111) SRTIO$_3$

$SrTiO_3$ was the first perovskite substrate to be singly terminated. The work on the preparation of these well-defined atomically flat surfaces was started by Kawasaki et al. and later refined by Koster et al. [39,40]. With new treatment methods atomically flat surfaces of (110) and (111) oriented $SrTiO_3$ were reported [41,42]. The ideal crystal structure of perovskite materials is described by two stacked sublayers, which, depending on the crystallographic orientation of the surface and the material's species, are either charge neutral or a polar. For $SrTiO_3$ (001) the sub-layers are SrO and $TiO_2$, which are both charge neutral. Both of these layers are very stable in terms of surface energy. For $SrTiO_3$ (110) the two sub-layers that make up the crustal structure are $SrTiO^{4+}$ and $O_2^{4-}$, which are both charged and have a high surface energy. First principle calculations suggest stability of Sr and Ti rich $SrTiO_3$ (110) surfaces for Ti and Sr poor environments, respectively [43]. For $SrTiO_3$ (111) the sub-layers are $SrO_3^{4-}$ and $Ti^{4+}$, which both have high surface energies due to the large dipole moment. Selective etching and annealing to create singly terminated surfaces has been previously suggested [44]. A schematic presentation of these sublayers is presented in Figure 7. No direct experimental evidence for single surface termination has been provided for either (110) or (111) oriented $SrTiO_3$ crystals. Using chemical etching and subsequent thermal annealing (001), (110), and (111) $SrTiO_3$ substrates were prepared with smooth terrace steps and using AR-MSRI the atomic composition of the surface was investigated [45].

Figure 8 shows the ratio between $Ti^+$ and $Sr^+$ AR-MSRI signals for both as-received and treated surfaces of (001), (110), and (111) $SrTiO_3$ substrates. For each of these crystal orientations the chemically etched and annealed surfaces there is an increased $Ti^+/Sr^+$ ratio and it is clear that the Ti-rich layer becomes dominant. The shadow cones of Ti cover Sr in the directions were peaks in the $Ti^+/Sr^+$ ratio are observed, 45° with 90° rotational symmetry for (001), -56° and -124° with 180° rotational symmetry for (110) and -90° with 120° rotational symmetry for (110). The relation between angles featured in the AR-MSRI data and crystalline directions can be obtained from Figure 7.
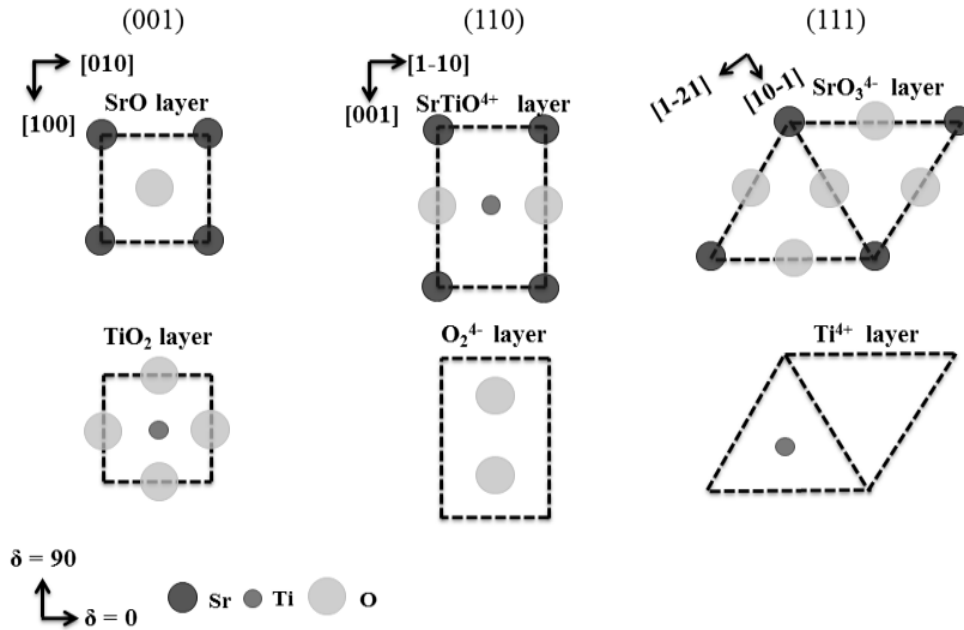
Figure 7. The sublayers that build up the (001), (110), and (111) oriented SrTiO$_3$ crystal structures.
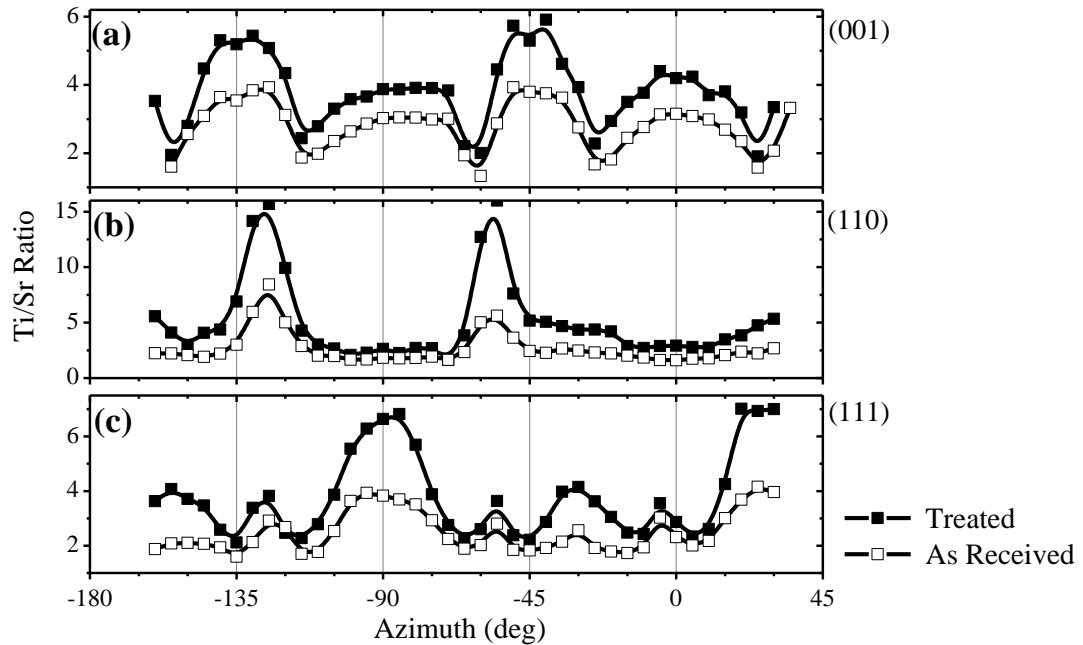


Figure 8. The ratio between Ti$^+$ and Sr$^+$ AR-MSRI signals for SrTiO$_3$. The (001), (110) and (111) orientations are presented in figure (a), (b) and (c) respectively. All plots show a comparison between substrates as they are supplied by the manufacturer (as received) and after the treatment.

For the (110) oriented surface $SrTiO_3$ the ideal surface is a $SrTiO^{4+}$ layer, which contains equal amounts of Sr and Ti. The enhancement in the $Ti^+/Sr^+$ ratio that is observed in the AR-MSRI data may be explained with a surface reconstruction model where $Sr^{2+}$ ions are missing, as considered by the theoretical work of Bottin et al. [43]. The relative intensities of $Ti^+$, $Sr^+$ and $O^+$ can be found in appendix 7.1.

### 3.1.2 LANTHANUM STRONTIUM ALUMINATE

Strontium lanthanum aluminate ($LaSrAlO_4$) is a popular substrate for epitaxial growth of high-$T_C$ superconducting thin films, which can be used for microwave and far-infrared applications [46]. $LaSrAlO_4$ has a perovskite-like $K_2NiF_4$ structure with lattice parameters a = b = 3.756 Å and c = 12.64 Å, and it has a high chemical stability [47]. It is build up by layers of Sr/LaO and $AlO_2$, where Sr and La are mixed and occupy the same lattice sites. A schematic of the crystalline structure is presented in Figure 9.
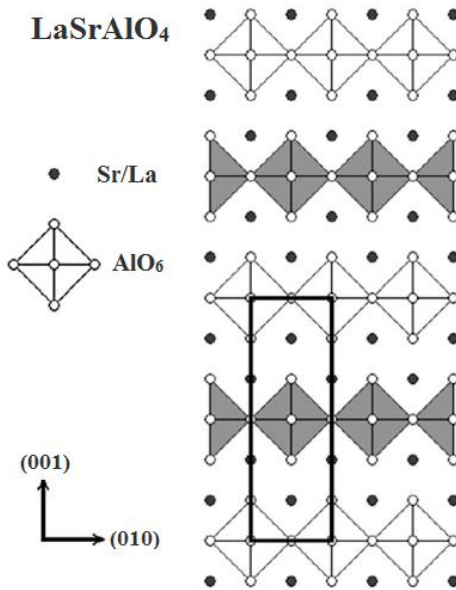


Figure 9. Schematic crystal structure of $LaSrAlO_4$.

While the properties of bulk samples of $LaSrAlO_4$ single-crystals have been studied extensively, the surface specific body of literature is limited to the study by Becerra-Toledo & Marks [48]. These authors report a segregation of strontium oxide (SrO) at the surface of single-crystal $LaSrAlO_4$ substrates annealed in oxidizing conditions. The SrO segregation is manifested in the appearance of islands on (100) and other high free energy surfaces. These particles create a significant roughness to the otherwise flat surface, possibly inhibiting well-defined epitaxial growth required for high quality thin films and devices. To facilitate the push forward in research by improving $LaSrAlO_4$ substrates, a method of surface treatment is required that prevents the creation of, or removes, the SrO particles, as well as creating an atomically defined smooth surface. Recently, it was discovered that smooth terrace surfaces can be achieved by annealing $LaSrAlO_4$ substrates with distinctive environments that are rich in the cations

22

included in the substrate. AR-MSRI and DRS are employed to determine whether these surfaces are singly terminated and, if so, what the topmost atomic layer is composed of [49].

In order to explore the composition of the LaSrAlO$_4$ surfaces AR-MSRI experiments were carried out. For insight in which of the planes of which the substrate is built up is the topmost layer the cationic ratio is analyzed. In the analysis one should remember that the LaSrAlO$_4$ structure is only perovskite like, not an actual perovskite. The double layer of Sr/LaO has a [½½0] displacement, which allows blocking and shadowing effects in [100] and [010] directions as well as [110] direction that is used for characterization of the topmost layer in perovskite materials. In Figure 10 the Al$^+$/(Sr$^+$+La$^+$) ratio is given for LaSrAlO$_4$ substrates as they were received from the supplier and substrates that went through an annealing process in La$_2$O$_3$ and LaAlO$_3$ environments. Using the signal of the as received sample as the baseline there is an overall decrease in the cationic ratio for the La$_2$O$_3$ sample, with the biggest reduction in the low index crystalline directions. These directions are marked by the 0° and 45° angles corresponding to [010] and [110] directions respectively. Although the general trend shows an oscillating signal with peaks at these angles, slight minima at the top of these oscillations can be observed. These features are indicating a shift towards the Sr/LaO as the topmost layer. For the LaAlO$_3$ sample an overall increase in the cationic ratio is observed, with the exception of the [010], or 0°, direction. The value of the ratio has the most dramatic increase in the [110], or 45°, direction, corresponding to shadowing of Sr/La by Al, indicating AlO$_2$ as the topmost layer. The minimum in the [010] direction suggests that Sr/LaO is the second layer.
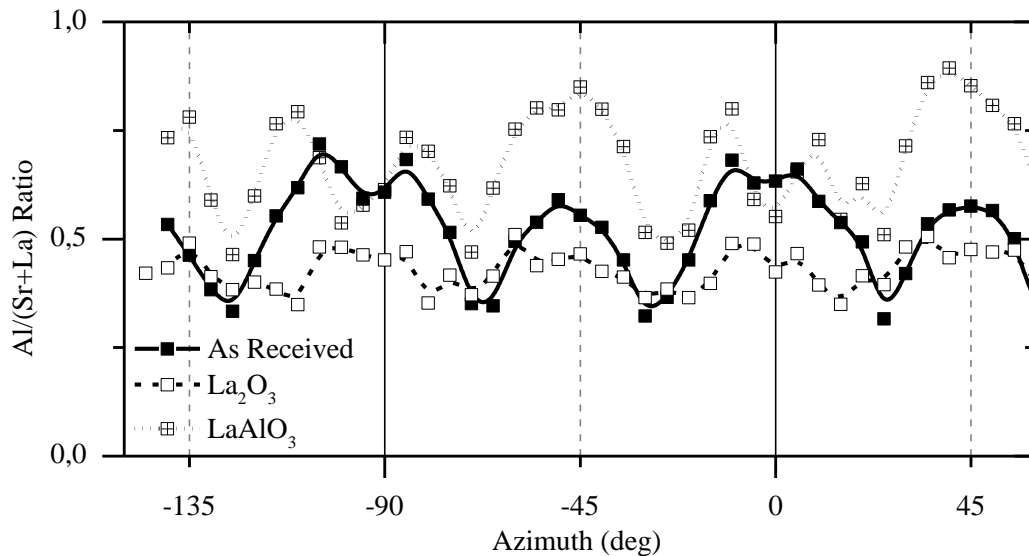


Figure 10. The ratio between the Al$^+$ signal and the combination of the Sr$^+$ and La$^+$ signals extracted from AR-MSRI experiments for LaSrAlO$_4$ substrates. Shown in the graph are the ratios for substrates as they were received from the supplier (filled squares and solid line) and substrates that went through an annealing process in La$_2$O$_3$ (empty squares and dashed line) and LaAlO$_3$ (cross squares and dotted line) environments. Of particular interest are the features along the low index crystalline directions.

For further insight in the cationic arrangement of the top layers of the LaSrAlO$_4$ substrates the ratios between the individual elements are plotted in Figure 11.
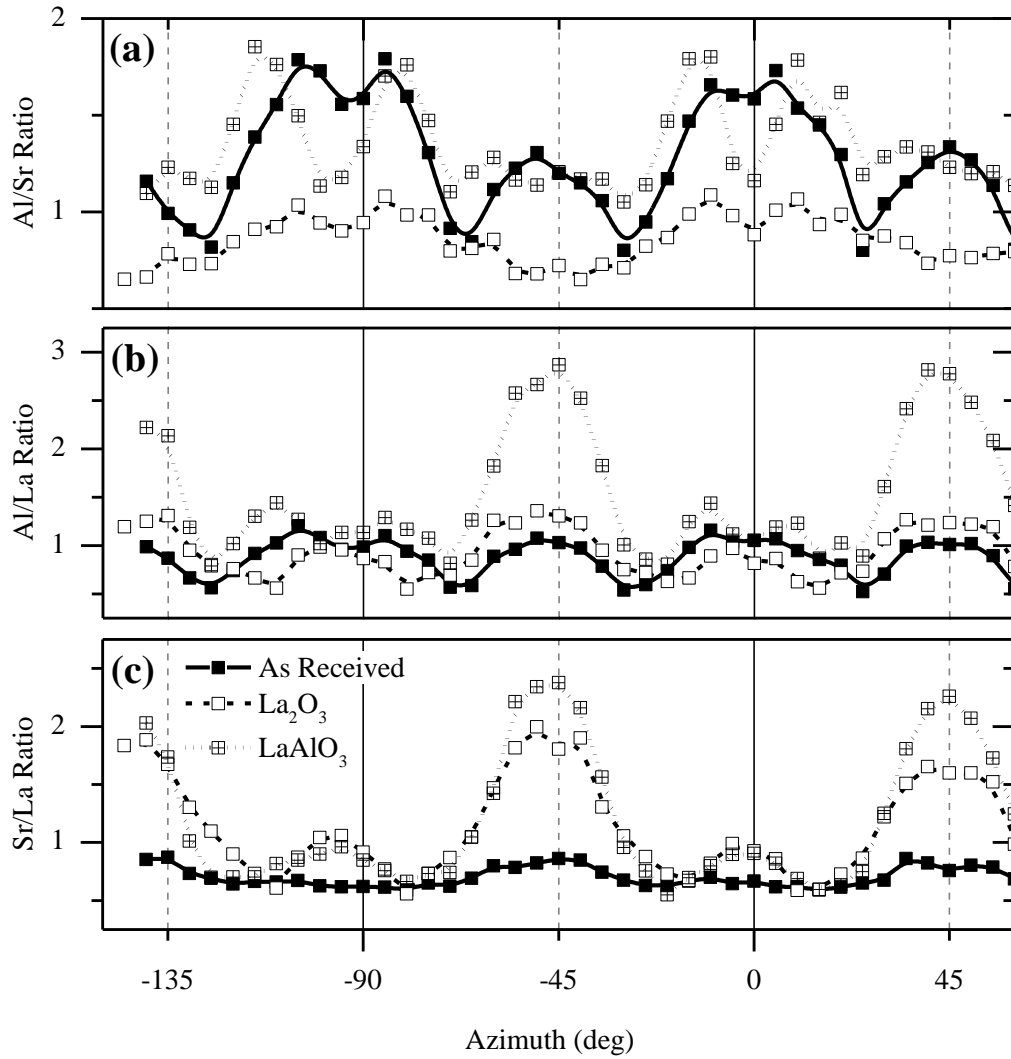


Figure 11. The ratios between the individual cations signals extracted from AR-MSRI experiments for LaSrAlO$_4$ substrates, (a) Al/Sr, (b) Al/La and (c) Sr/La, respectively. The different substrates are marked by filled squares and solid line for 'as received' substrates, empty squares and dashed line for La$_2$O$_3$ annealing environment, and cross squares and dotted line for LaAlO$_3$ annealing environments. Of particular interest are the features along the low index crystalline directions.

For the as received $LaSrAlO_4$ sample the $Al^+/Sr^+$ and $Al^+/La^+$ ratios show the same features as the overall cationic ratio, and the $Sr^+/La^+$ shows almost no modulation. This indicates that there is good mixing of Sr and La in the Sr/LaO layer on the surface. The $La_2O_3$ sample features distinctive minima for the $Al^+/Sr^+$ ratio in the [110] direction, evidencing the shadowing of Al by Sr. The low intensity peaks for all low index crystalline directions for the $Al^+/La^+$ ratio suggest that there is no La on top of the first $AlO_2$ layer. The strong maximum along [110] direction for the $Sr^+/La^+$ ratio indicates that the topmost layers of the $La_2O_3$ sample are La poor. The $LaAlO_3$ sample has increased values for the $Al^+/Sr^+$ ratio and strong maxima for the $Al^+/La^+$ ratio in the [110] direction, indicating shadowing of both La and Sr by Al and therefore evidencing $AlO_2$ to be the topmost layer. The minimum in the both the $Al^+/Sr^+$ and $Al^+/La^+$ ratios in the [010] direction indicates only a single layer of $AlO_2$ at the top. The appearance of [110] direction maxima for the $Sr^+/La^+$ ratio suggests La poor surface layers. From comparing the $Sr^+/La^+$ ratio signals for the three different samples it can be concluded that the annealing process results in La-poor Sr/LaO layers at the surface of the $LaSrAlO_4$ crystal.

For corroboration of the AR-MSRI conclusions the DRS data is analyzed, which was collected simultaneously. In Figure 12 the TOF spectrum is shown for the $La_2O_3$ and $LaAlO_3$ samples in both [010] and [110] directions, at 0° and 45° respectively. In these spectra the signals for recoiled hydrogen ($H_R$) and oxygen ($O_R$) as well as scattered potassium ($K_S$) are easily identified. A closer look at the $K_S$ signal reveals two peaks. When scattering off a heavy elements, such as Sr and La, the primary ions retain much more of their kinetic energy than when scattering off a light element, such as Al. Therefore the $K_S(1)$ peak is allocated to Sr and La, and the $K_S(2)$ peak to Al.
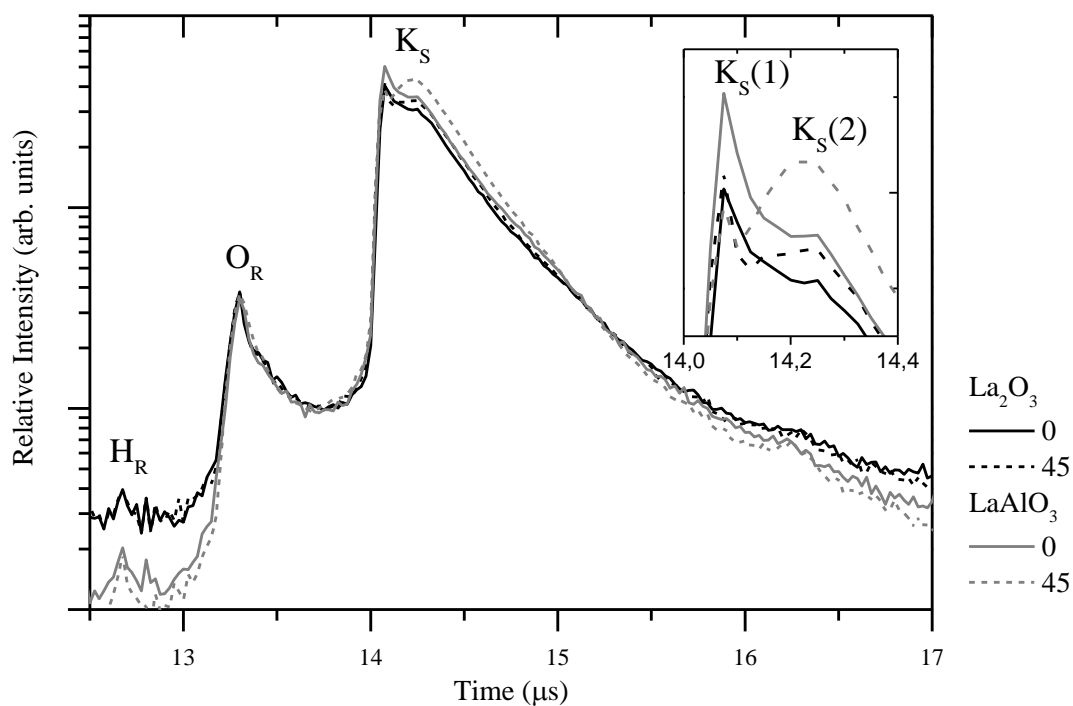
Figure 12. The DRS spectra for LaSrAlO$_4$ substrates annealed in La$_2$O$_3$ (black) and LaAlO$_3$ (grey) atmosphere, along azimuthal angles of 0 (solid) and 45 (dashed) degrees. The peaks for recoiled hydrogen (H$_R$) and oxygen (O$_R$) atoms are labeled on the left, and the scattered potassium (K$_S$) peak is labeled in the center. The inset shows the two peaks that can be distinguished in K$_S$ peak region. Note that the noise level varies significantly between measurements, as can be observed at the intersection with the y-axis.

The relative intensities of the K$_S$(1) and K$_S$(2) peaks as a function of the azimuthal angle are plotted in Figure 13. La$_2$O$_3$ sample has a significant overall increase of the K$_S$(1) peak, indicating the Sr/LaO layer to become more dominant at the surface in respect to both the as received and LaAlO$_3$ samples. In the K$_S$(2) peak's case it is the LaAlO$_3$ sample which features an overall intensity increase, indicating the AlO$_2$ layer to become more dominant at the surface in respect to both the as received and La$_2$O$_3$ samples. The intensities of the H$_R$ and O$_R$ signals are included in Appendix 7.4.
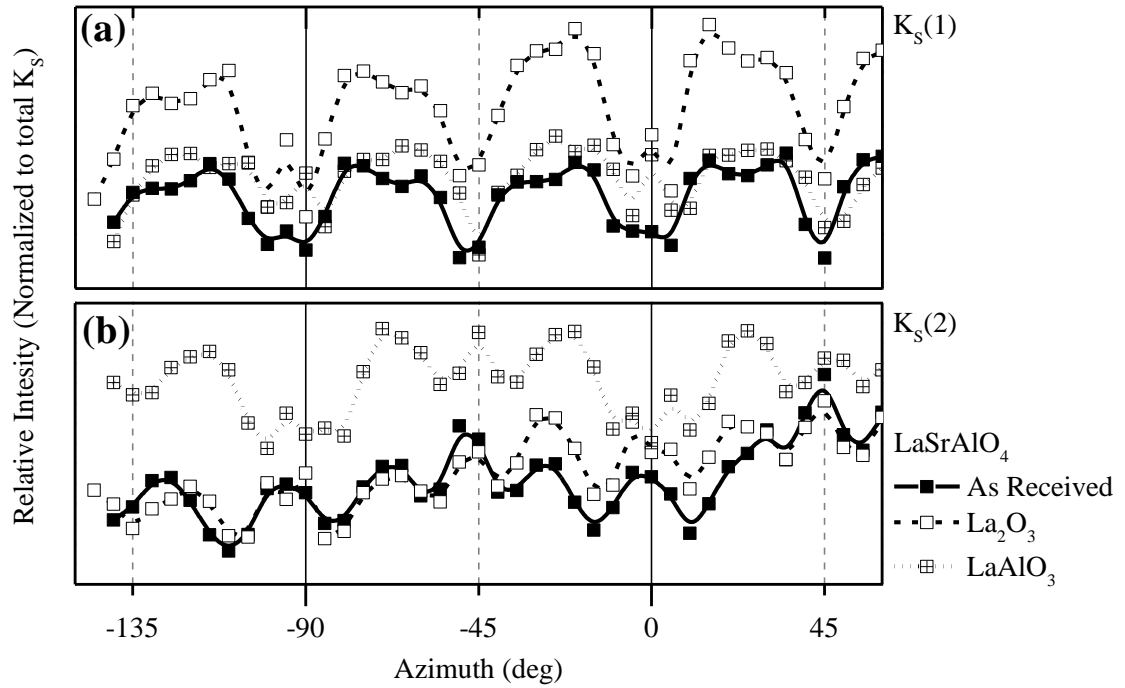
Figure 13. The normalized relative intensity values of $K_S(1)$ (a) and $K_S(2)$ (b) as a function of the azimuthal angle, with filled squares and solid line for 'as received' substrates, empty squares and dashed line for $La_2O_3$ annealing environment, and cross squares and dotted line for $LaAlO_3$ annealing environments.

## 3.2 Material's composition and stoichiometry

The quality and properties of devices is strongly dependent on the composition of the thin films they are made of. Stringent limits on the presence of unwanted defects and precise control of doping are required to ensure device quality and reproducibility. The uncontrolled presence of defects influences and often dominates the properties of oxides. Using natural minerals for the realization of low cost energy conversion and storage devices has become the objective to take the challenge of energy consumption. The presence of various impurities results in components with degraded performance. Insight into the chemical composition of the material is necessary to devise ways to achieve increase in performance. In this section analyses of the transfer of dopant species from the target to the substrate in the pulsed laser deposition (PLD) process and the influence of ambient pressure during the deposition on the stoichiometry are presented.

### 3.2.1 MALACHITE

$Cu_2O$ is a good candidate for low cost solar cell applications, with p-type absorber properties. It is a cheap, abundant, non-toxic oxide material and it has good hole mobility, large minority carrier diffusion length, and a direct energy gap ideal for efficient absorption. Malachite, copper carbonate copper hydroxide, is a common copper ore with

27

a composition $Cu_2CO_3(OH)_2$ [50]. To characterize impurities present in the malachite mineral and the transfer to the substrates in the PLD process both the target and a film grown on a LSAT (001) substrate are analyzed by MSRI, the resulting mass spectra are presented in Figure 14 [51].
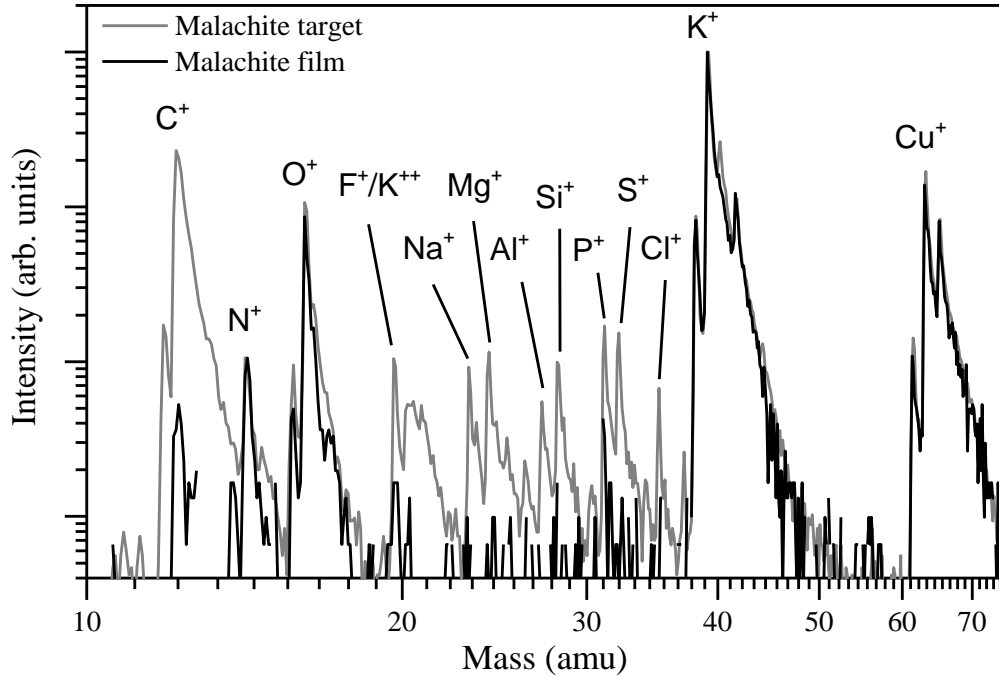


Figure 14. The MSRI spectra at $\alpha = 15°$ for the malachite target (dotted grey line) and a malachite film (straight black line), note that the intensity is plotted on a log scale.

The malachite mineral target is ideally composed of copper, carbon and oxygen atoms, and each of these elements has a strong peak associated with it. Other elements found in the mineral, with a much lower relative intensity, are fluorine, sodium, magnesium, aluminum, silicon, phosphorus, sulfur and chlorine. A qualitative assessment of the surface chemical composition of the grown malachite film reveals the presence of copper and oxygen mainly. Despite its strong presence in the malachite mineral target is not transferred to the substrate during the PLD process. The impurities found in the target and named above also do not transfer to the substrate.

### 3.2.2 CATION VACANCIES IN SrTiO₃

The stoichiometry of films produced by PLD, often the method of choice for growing oxides, has been argued to be dependent on the ablation parameters used in the growth process [52]. The dominant point defects in $SrTiO_3$ are vacancies and their complexes, and differences in densities of these defects have a striking impact on film properties [53]. Oxygen vacancies are commonly attributed to the growth pressure, and,

since they are electron donors, can be characterized by analyzing the film's electrical properties [54]. Cation vacancies, $V_{Ti}$ and $V_{Sr}$, in both sub layers of $SrTiO_3$ have been identified as a function of laser fluence [53]. Recent first principle calculations show an increased energetic stability for $V_S$ (but not $V_{La}$ or $V_{Ti}$) at high oxygen pressure [55]. The absence experimental evidence for the dependence of cationic stoichiometry on oxygen growth pressure provided the incentive for investigating this system with AR-MSRI. For these experiments 7 unit cell layers of $Sr_{1-x}La_xTiO_3$ (x = 0 and x = 0.15) were grown on LSAT (001) substrates using PLD. These depositions were done at both low pressure ($\sim 10^{-6}$ Torr $H_2O$ and $<10^{-7}$ Torr $O_2$ at 850°C) and at high pressure ($>10^{-1}$ Torr $O_2$).

To investigate a shift in the ratio between cationic vacancies (i.e. $V_{Ti}/(V_{Sr}+V_{La})$) the ratio between the AR-MSRI signals is plotted in Figure 15. By focusing the attention on the [010] direction, corresponding to $\delta = 0$, the influence of shadowing effects between the cations, which could be the result of variations in surface termination, is minimized. A trend is readily observed, the $Ti^+/(Sr^++La^+)$ ratio is higher films grown under high pressure than it is for films grown under low pressure, for both $La_{0.15}Sr_{0.85}TiO_3$ and $SrTiO_3$. This trend can be explained by (a combination of) various phenomena. An increased $V_{Sr}$ (and possibly $V_{La}$) density for high pressures as well as an increased $V_{Ti}$ density for low pressures would result in the observed trend. In order to determine which of these phenomena is responsible for the observed trend the relative intensities of the individual elements are analyzed.



| Average Ti/(Sr+La) Ratio | |
| --- | --- |
| ($\alpha$ = 15, $\delta$ = -10 to 10) | |
| Pressure | La-SrTiO |
| High | 2,15 ± 0.07 |
| Low | 1.86 ± 0.07 |
| Pressure | SrTiO |
| High | 1,82 ± 0.04 |
| Low | 1.47 ± 0.10 |

- ■ $La_{0.15}Sr_{0.85}TiO_3$ - High pressure
- □ $La_{0.15}Sr_{0.85}TiO_3$ - Low pressure
- ◆ $SrTiO_3$ - High pressure
- ◇ $SrTiO_3$ - Low pressure
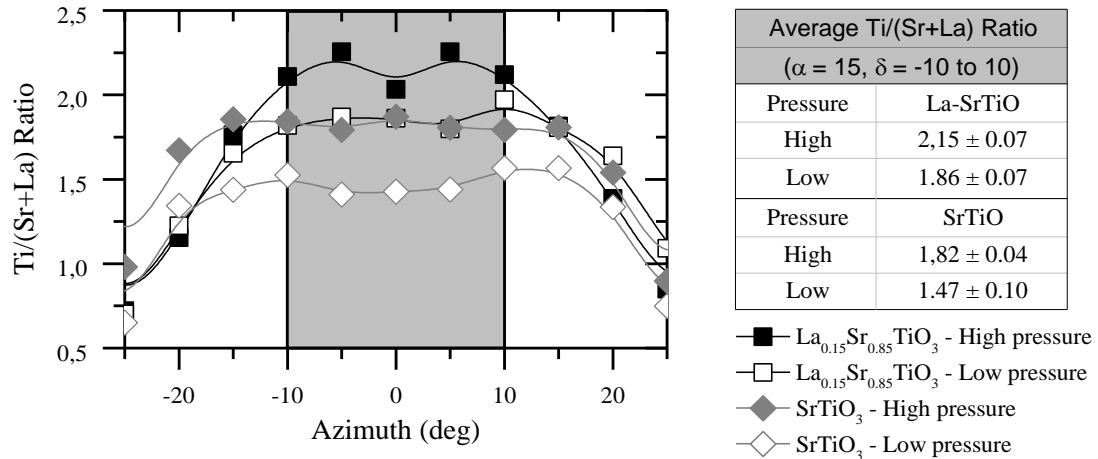
Figure 15. The experimental values of the cationic ratio, $Ti^+/(Sr^++La^+)$, from AR-MSRI experiments are presented as a function of azimuthal angle. The average and standard deviation of the cationic ratio for $Sr_{0.85}La_{0.15}TiO_3$ (squares) and $SrTiO_3$ (diamonds) films are compared around the [010] direction (shaded region), where there are no shadowing effects between the two sub-layers.

In Figure 16 the relative intensities of $Sr^+$ and $Ti^+$ in $SrTiO_3$ are presented. The used angles of incidence ($\alpha$) are 15° and 30°, where in the 30° case the shadowing and blocking cones are directed more downward, which is expected reduce the sensitivity to the topmost layer only. The $Sr^+$ signal shows significant decreases for high pressures, particularly for $\alpha = 30°$, whereas the $Ti^+$ signal is similar for high and low pressures. The

angles in which the $Sr^+$ and $Ti^+$ signals have peak values is expected to have the lowest signal to noise ratio and the least influence by other elements. The difference in these peak values is very strong for $Sr^+$, whereas it is minimal for $Ti^+$, indicating that $V_{Sr}$ are responsible for the observed trend in the cationic ratio.
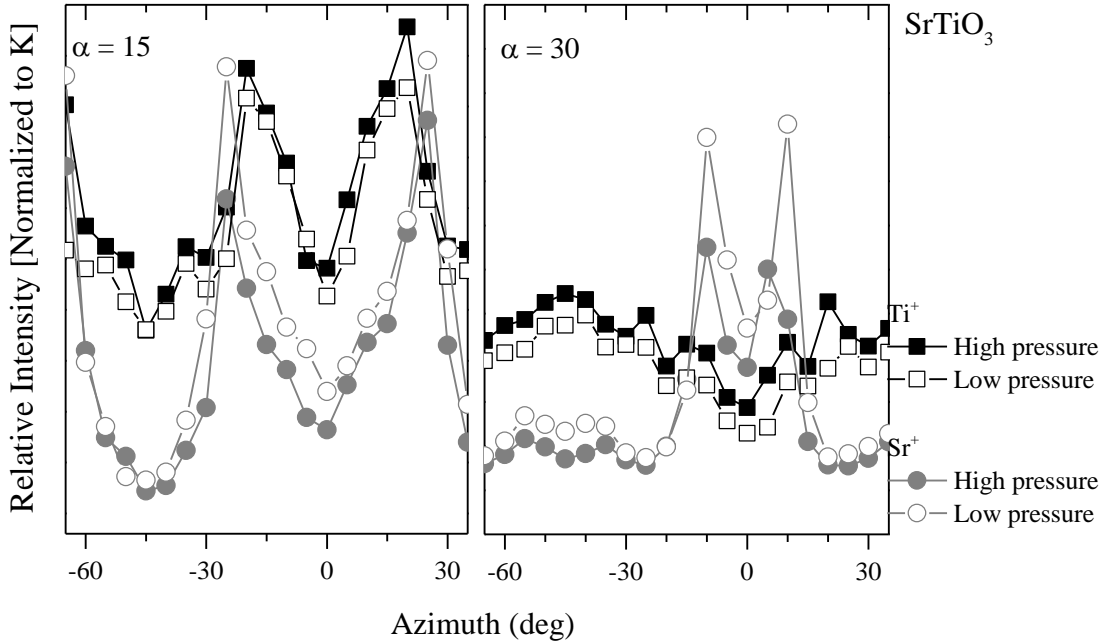


Figure 16. The relative intensities from AR-MSRI for $Ti^+$ (black squares) and $Sr^+$ (grey circles) for $SrTiO_3$ films grown at high (filled) and low (open) pressures, $\alpha = 15°$ and $\alpha = 30°$ are shown on the left and on the right, respectively. Not the significant decrease in intensity for the $Sr^+$ signals for high pressure at the peak angles.

For the $La_{0.15}Sr_{0.85}TiO_3$ films the relative intensities of recoiled $La^+$ and $Sr^+$ are compared to provide insight in the density ratio between $V_{La}$ and $V_{Sr}$. The AR-MSRI spectra are shown incident angles of 15° and 30° in Figure 17. While the $La^+$ signal is similar for the two growth pressures, a clear difference is observed in the $Sr^+$ signal. The $Sr^+$ relative intensity is higher at low pressures, suggesting that growth at low pressures results in the incorporation of more Sr into the films. Combined the increased $Ti^+/(Sr^++La^+)$ ratio for films grown under high pressure and the decrease in the $Sr^+$ compared to $La^+$ in $La_{0.15}Sr_{0.85}TiO_3$ and $Ti^+$ in $SrTiO_3$ make up compelling evidence for energetically favorable $V_{Sr}$ at high growth pressures.
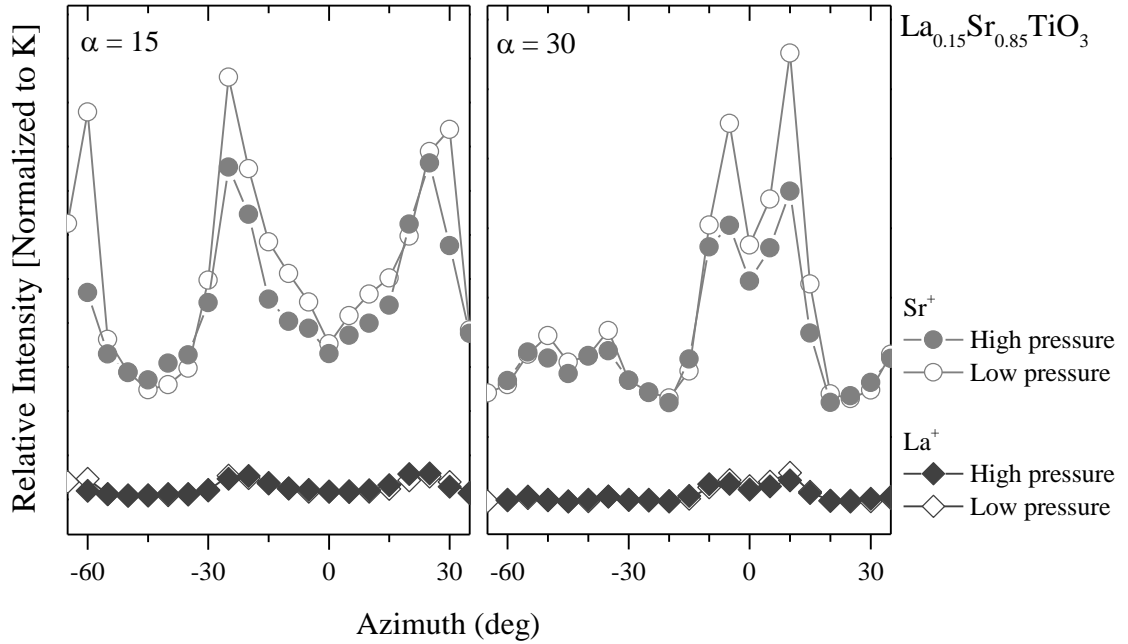
Figure 17. The relative intensities from AR-MSRI for $La^+$ (dark grey diamonds) and $Sr^+$ (grey circles) for $La_{0.15}Sr_{0.85}TiO_3$ films grown at high (filled) and low (open) pressures, $\alpha = 15°$ and $\alpha = 30°$ are shown on the left and on the right, respectively. Not the significant decrease in intensity for the $Sr^+$ signals for high pressure.

## 3.3 Surface composition of SrTiO₃ and LaAlO₃ films

The growth of perovskite lanthanum aluminate, $LaAlO_3$, films on $TiO_2$-terminated $SrTiO_3$ substrates took off when Ohtomo and Hwang presented the claim of a high-mobility electron gas at the $LaO/TiO_2$ interface [29]. The thickness dependence of the transport properties was investigated and it was found that only four monolayers are necessary to go from insulating to metallic behavior [56]. Various groups use PLD for the growth of films of $LaAlO_3$ to investigate the properties of the two possible hetero-epitaxial interface configurations [57]. These studies investigating the $SrTiO_3/LaAlO_3$ interface employ PLD for changing the termination on $TiO_2$ terminated $SrTiO_3$ substrates and the growth of $SrTiO_3$ buffer layers, as well as the growth of the $LaAlO_3$ film. In most cases in-situ RHEED and transport properties of the $SrTiO_3/LaAlO_3$ devices are the only means of surface characterization. The absence of a comparative study using a surface sensitive characterization technique presents an opportunity for TOF-ISARS to investigate the differences between $TiO_2$ and $SrO$ terminated $SrTiO_3$ that are produced by PLD.

Whereas the two sublayers of $SrTiO_3$ are neutral the sublayers of $LaAlO_3$, $AlO_2$ and $LaO$ are both charged, creating a dipole at the crystal surface whatever the

31

terminating layer. There have been experimental as well as theoretical studies investigating the termination and reconstructions of LaAlO$_3$ single crystals. Using ion scattering experiments determined it was claimed that LaAlO$_3$ crystals terminate exclusively in an AlO$_2$ layer up to ~150 °C and exclusively in a LaO layer at temperatures above ~250 °C [58]. The room temperature termination by AlO$_2$ was confirmed by X-ray truncation rod analysis [59]. Another study, employing, neutral scattering spectroscopy, determined that below room temperature both terminations exist [60]. Using molecular dynamics simulations LaO termination was determined to be more stable than the AlO$_2$ termination [61]. Through transmission electron diffraction and density functional calculations it was claimed that at room temperature LaAlO$_3$ has an AlO$_2$ termination with additional oxygen layer on top (but no La), and that the surface contains no oxygen vacancies or hydrogen occupying the empty La sites. Holes in the film are suggested as the compensation of the surface dipole [62]. An experimental study employing PLD and sputtering, aided by classical and quantum mechanical calculations, showed that LaAlO$_3$ grown on TiO$_2$-terminated SrTiO$_3$ (001) exhibits strong cation intermixing [63]. During the growth downhill diffusion of LaAlO$_3$ to the SrTiO$_3$ substrate to the LaAlO$_3$ film was found to be energetically favorable. All activation barriers were found to decrease for increasing thickness of the LaAlO$_3$ layer and the diffusion barriers are small compared to homo-epitaxial SrTiO$_3$ [64]. The ambiguity among LaAlO$_3$ crystal termination studies and to complete lack of experimental or theoretical studies focusing on the surface of LaAlO$_3$ films was the motivation for employing TOF-ISARS to investigate film grown on TiO$_2$ and SrO terminated SrTiO$_3$ by PLD.

### 3.3.1 SRO AND TIO$_2$ TERMINATED SRTIO$_3$

For the investigation by TOF-ISARS TiO$_2$ and SrO terminated surfaces where created by PLD. The commonly employed interval deposition technique could not be employed, due to limitations in the setup of the PLD chamber. To create the SrO termination a single layer of strontium ruthanate, which is known to terminate with a SrO layer regardless of the bottom layer, was grown on TiO$_2$ terminated SrTiO$_3$ [65]. This was followed by the growth of 5 monolayers of SrTiO$_3$. In order to maximize the comparability the same number of monolayers SrTiO$_3$ was grown on the TiO$_2$ terminated substrate.

The Ti$^+$/Sr$^+$ ratio AR-MSRI of both films as well as a mixed termination substrate is presented in Figure 18. The analysis of these graphs is follows that of paragraph 3.1.1 and should focus on the [110] direction along the 45° angle. The trends in both directions are clear and confirm the presence of a Ti rich surface in one case and Sr rich in the other.
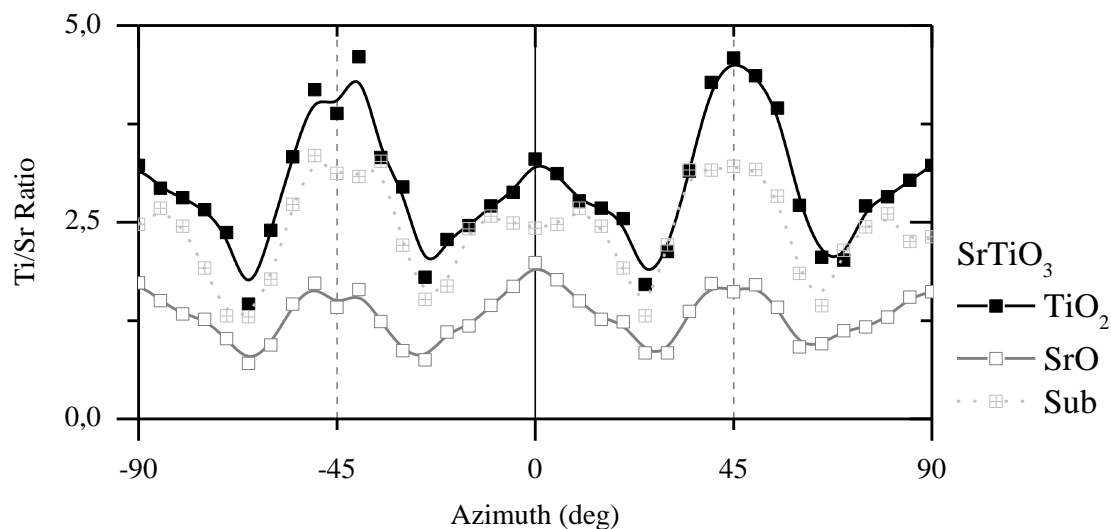
Figure 18. The Ti$^+$/Sr$^+$ ratio extracted from AR-MSRI experiments for SrTiO$_3$. Shown in the graph are the ratios for TiO$_2$-SrTiO$_3$ (filled squares and solid line), SrO-SrTiO$_3$ (empty squares and solid line) and an as received substrate with mixed termination (crossed squares and dotted line).
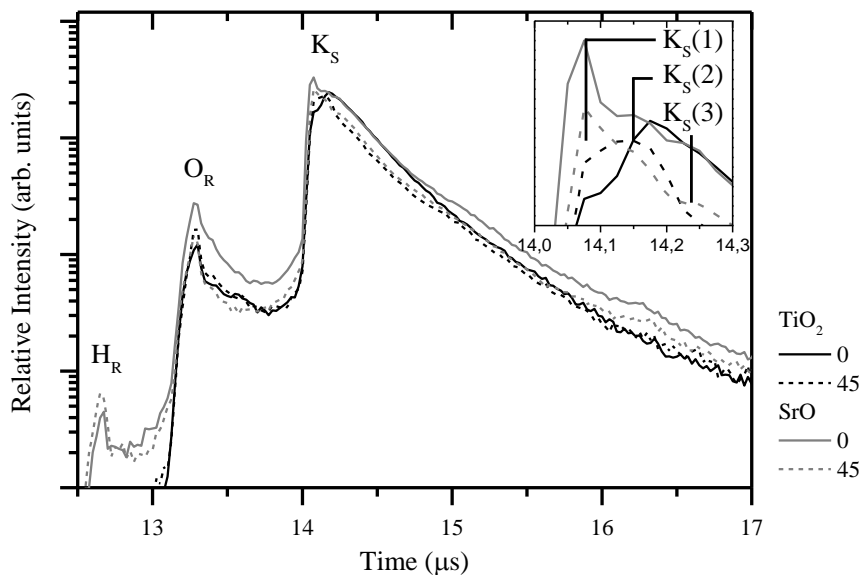


Figure 19. The DRS spectra for TiO$_2$- (black) and SrO-SrTiO$_3$ (grey) films, along azimuthal angles of 0 (solid) and 45 (dashed) degrees. The peaks for recoiled hydrogen (H$_R$) and oxygen (O$_R$) atoms are labeled on the left, and the scattered potassium (K$_S$) peak is labeled in the center. The inset shows the three peaks that can be distinguished in K$_S$ peak region.

To analyze the DRS data the signals of interested are extracted from the full TOF spectra as presented in Figure 19. The peaks corresponding to recoiled hydrogen (H$_R$) and oxygen (O$_R$) as well as scattered potassium (K$_S$) are identified. Detailed observation of

33

the $K_S$ signal reveals three peaks. Based on the mass of the elements in $SrTiO_3$ the $K_S$ peaks are assigned as: $K_S(1)$ to Sr, $K_S(2)$ to Ti and $K_S(3)$ to O. In Figure 20 the angular dependent spectra for the $K_S$ signals are plotted. Although the overall shape is similar for the $K_S(1)$ spectra the values are higher for the $SrO$-$SrTiO_3$, especially at 0° where no shadowing of Sr by O occurs. The most significant differences, however, are present in the $K_S(2)$ and $K_S(3)$ spectra. $K_S(2)$, associated with Ti, doesn't exhibit the deep minima at 45° when $TiO_2$ is the terminating layer, due to the absence of shadowing by both O and Sr. The minima at 0° and 23° can be explained by increased shadowing and blocking of the O in the surface layer, which is subject to an elevation of 0.1Å [21]. The $K_S(3)$, associated with O, is almost the direct inverse of $K_S(1)$ in the $SrO$-$SrTiO_3$ case and $K_S(2)$ in the $TiO_2$-$SrTiO_3$ case, which confirms single termination in both cases.



Figure 20. The normalized relative intensity values of $K_S(1)$ (a), $K_S(2)$ (b) and $K_S(3)$ (c) as a function of the azimuthal angle, with filled squares for $TiO_2$-$SrTiO_3$ and empty squares $SrO$-$SrTiO_3$.

The $H_R$ and $O_R$ spectra are shown in Figure 21. The $O_R$ is clearly different for the two terminations and the additional local minimum at ~20° for $TiO_2$-$SrTiO_3$ is explained by the shadowing among O atoms in the [310] direction, which is unique for the $TiO_2$

termination. Additional proof of the SrO termination is presence of hydrogen atoms at the surface, since SrO is known for its reaction with water to form $Sr(OH)_2$, while it is unlikely that water reacts with the very stable $TiO_2$ layer [40].
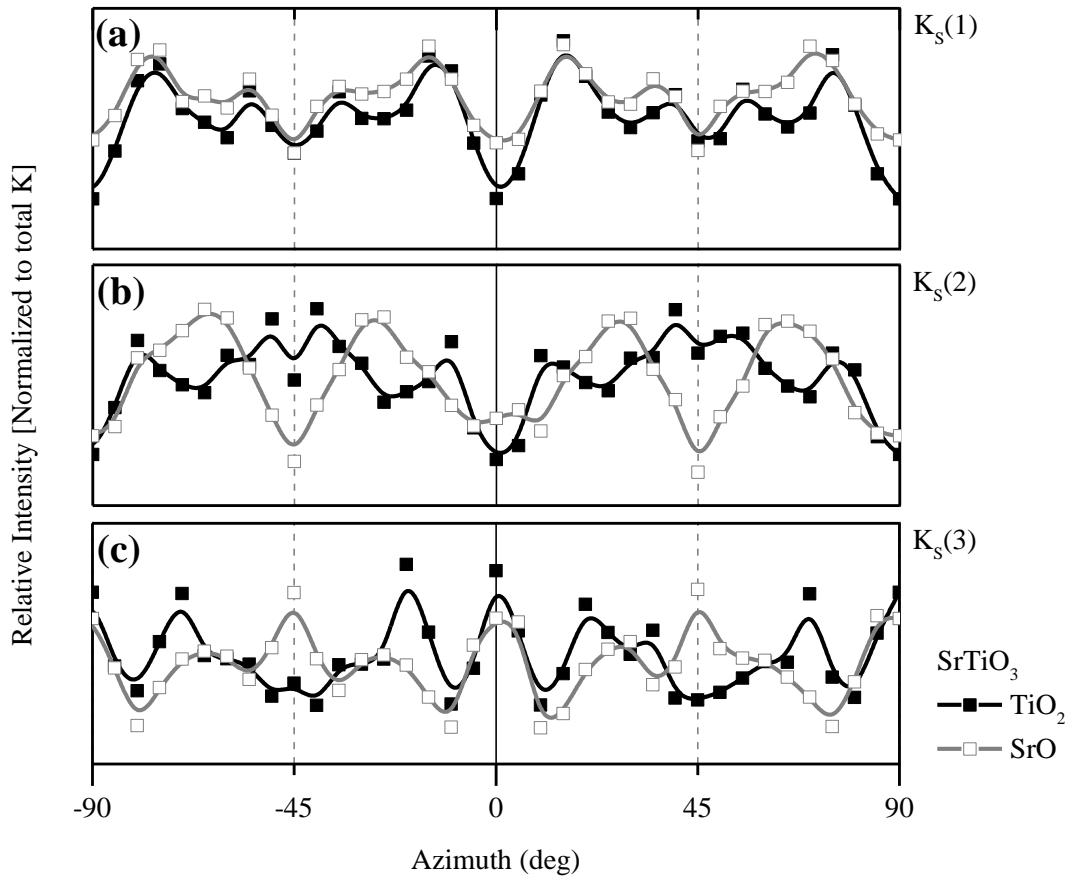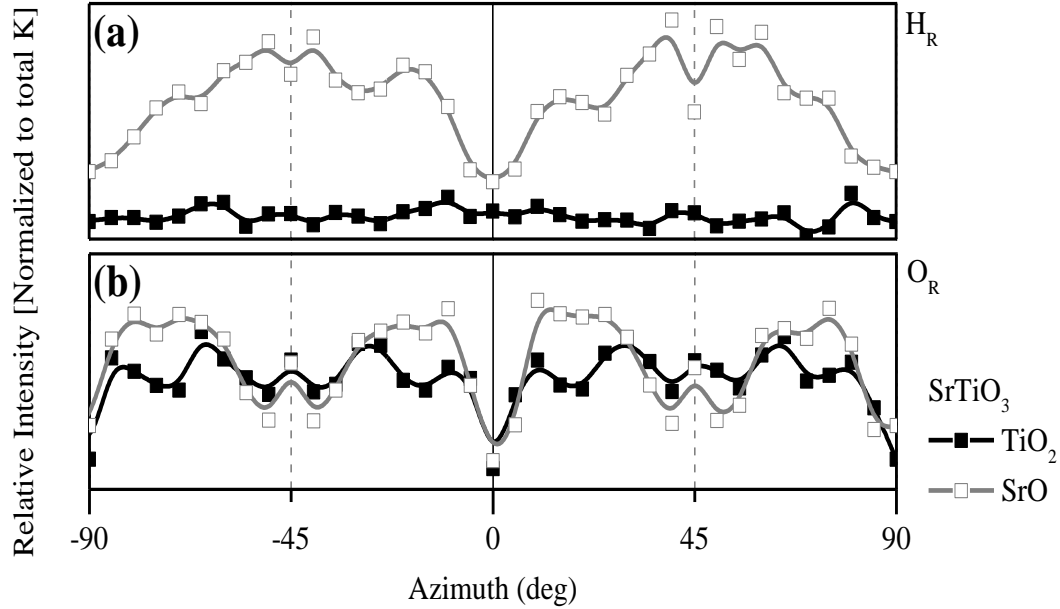


Figure 21. The normalized relative intensity values of $H_R$ (a) and $O_R$ (b) as a function of the azimuthal angle, with filled squares for $TiO_2$-$SrTiO_3$ and empty squares $SrO$-$SrTiO_3$.

### 3.3.2 EPITAXIAL LaAlO₃ FILMS ON SrTiO₃

With the experimental evidence of both SrO and $TiO_2$ terminated $SrTiO_3$, the investigation of $LaAlO_3$ films on two different terminations was started. Since the same system is used for the TOF-ISARS experiments and thin film growth, the singly terminated $SrTiO_3$ surfaces were not exposed to the atmosphere.

The $Al^+/La^+$ ratio for films grown on SrO and $TiO_2$ layers are shown in Figure 22. The values at 45°, where Al and La can shadow each other, are similar for films grown on both surfaces and indicating an $AlO_2$ terminating layer. The lower values around 0° for $LaAlO_3$ films grown on SrO can be explained by the presence of (partially filled) LaO layer without the La atoms at the surface, as the Al would be shadowed by these O atoms.

To further investigate the surface composition of the $LaAlO_3$ films the $O^+$ signal from the AR-MSRI experiment is analyzed, shown in Figure 23. Whereas there are distinct differences between the $O^+$ spectra for SrO and $TiO_2$ terminated $SrTiO_3$, the shape of $O^+$ spectra for the $LaAlO_3$ films grown on these surfaces are almost identical. In the low index crystalline directions, around 0° and 45°, the difference between sets for $LaAlO_3$ and $SrTiO_3$ surfaces is striking. With low minima around 0° and minima with moderate intensities around 45° the spectra for the $LaAlO_3$ films are most similar to that of $TiO_2$ terminated $SrTiO_3$.

35
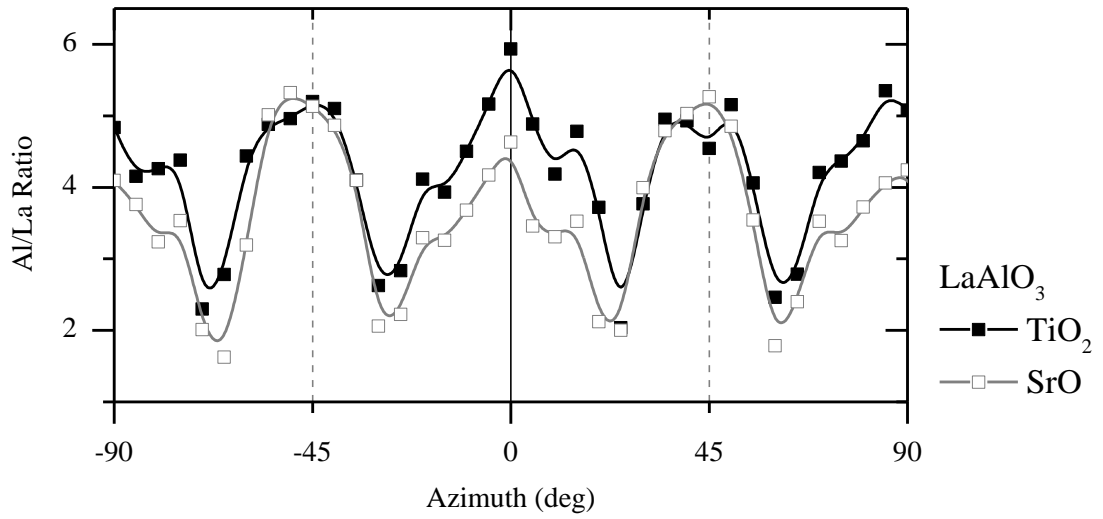
Figure 22. The $Al^+/La^+$ ratio extracted from AR-MSRI experiments for $LaAlO_3$. Shown in the graph are the ratios for films grown on $TiO_2$-$SrTiO_3$ (filled squares and solid line) and on $SrO$-$SrTiO_3$ (empty squares and solid line).
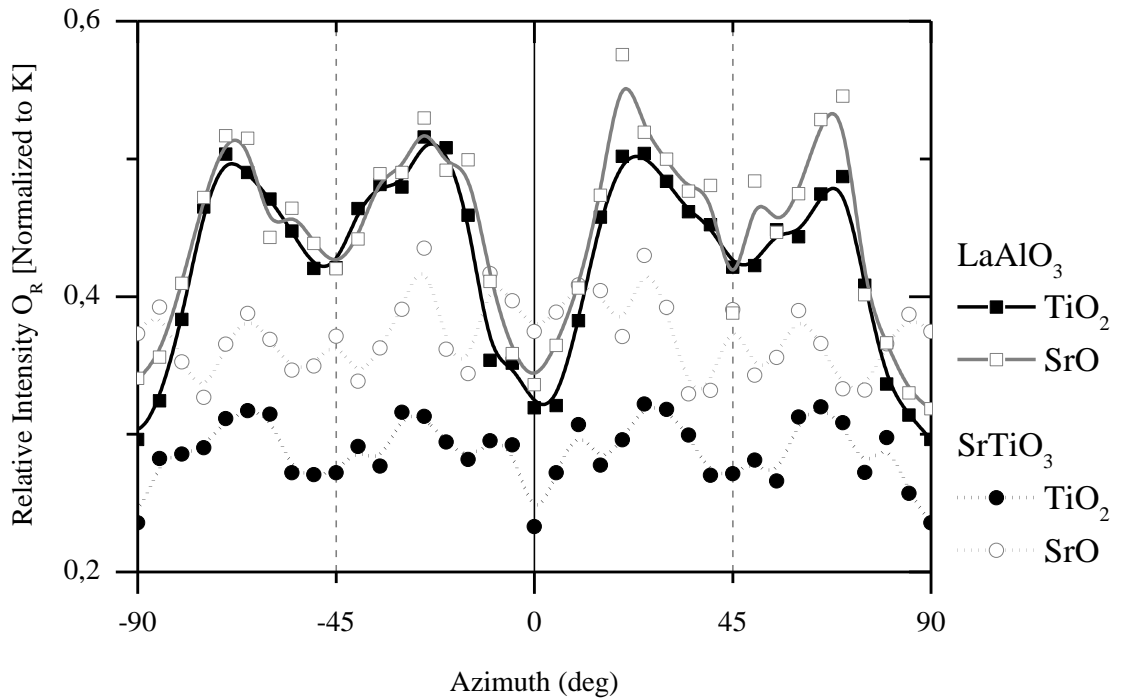


Figure 23. The relative intensity of $O^+$ is presented for $LaAlO_3$ films grown on $TiO_2$ (filled squares and solid line) and on $SrO$ (empty squares and solid line), as well as the $TiO_2$-$SrTiO_3$ (filled circles and dotted line) and on $SrO$-$SrTiO_3$ (empty circles and dotted line) surfaces themselves.

The TOF spectra of the DRS can be found in Figure 24, along with the peak allocation of recoiled oxygen ($O_R$) and aluminum ($Al_R$), and potassium scattered off La ($K_S(1)$) and off Al ($K_S(2)$). Due to the small mass difference with Al no scattering peak could be identified for O. The signal for recoiled hydrogen did not sufficiently exceed the noise level for it to be considered here. The AR-DRS data is presented in Figure 25. The spectra for all of the signals are almost identical for films grown on SrO and $TiO_2$ terminated $SrTiO_3$. Both $K_S(2)$ and $Al_R$ feature maxima at $\pm45°$ indicating $AlO_2$ termination. Based on both the AR-MSRI and AR-DRS analysis it can be concluded that thin $LaAlO_3$ films grown on both SrO and $TiO_2$ terminated $SrTiO_3$ terminates in a $AlO_2$ layer.
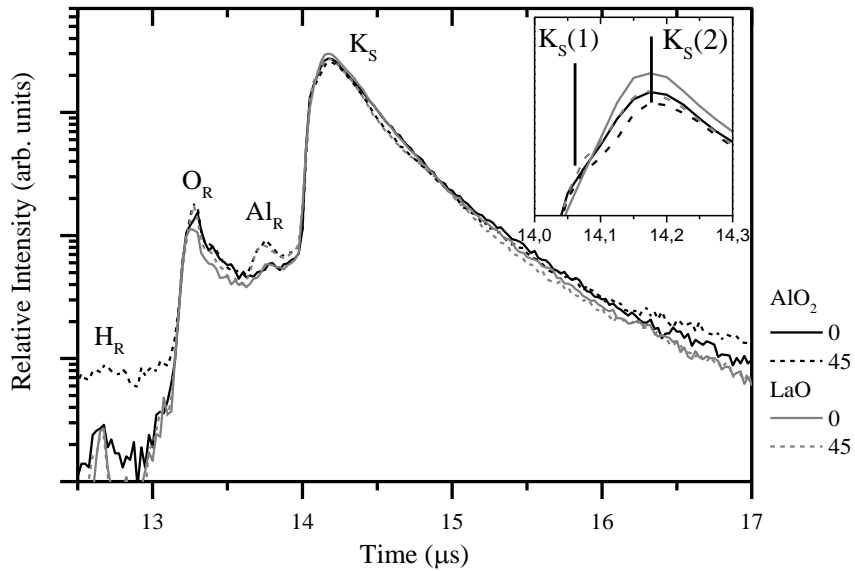


Figure 24. The DRS spectra for $LaAlO_3$ films grown on $TiO_2$- (black) and SrO-$SrTiO_3$ (grey), along azimuthal angles of 0 (solid) and 45 (dashed) degrees. The peaks for recoiled hydrogen ($H_R$), oxygen ($O_R$) and Aluminum ($Al_R$) atoms are labeled on the left, and the scattered potassium ($K_S$) peak is labeled in the center. The inset shows the two peaks that can be distinguished in $K_S$ peak region.
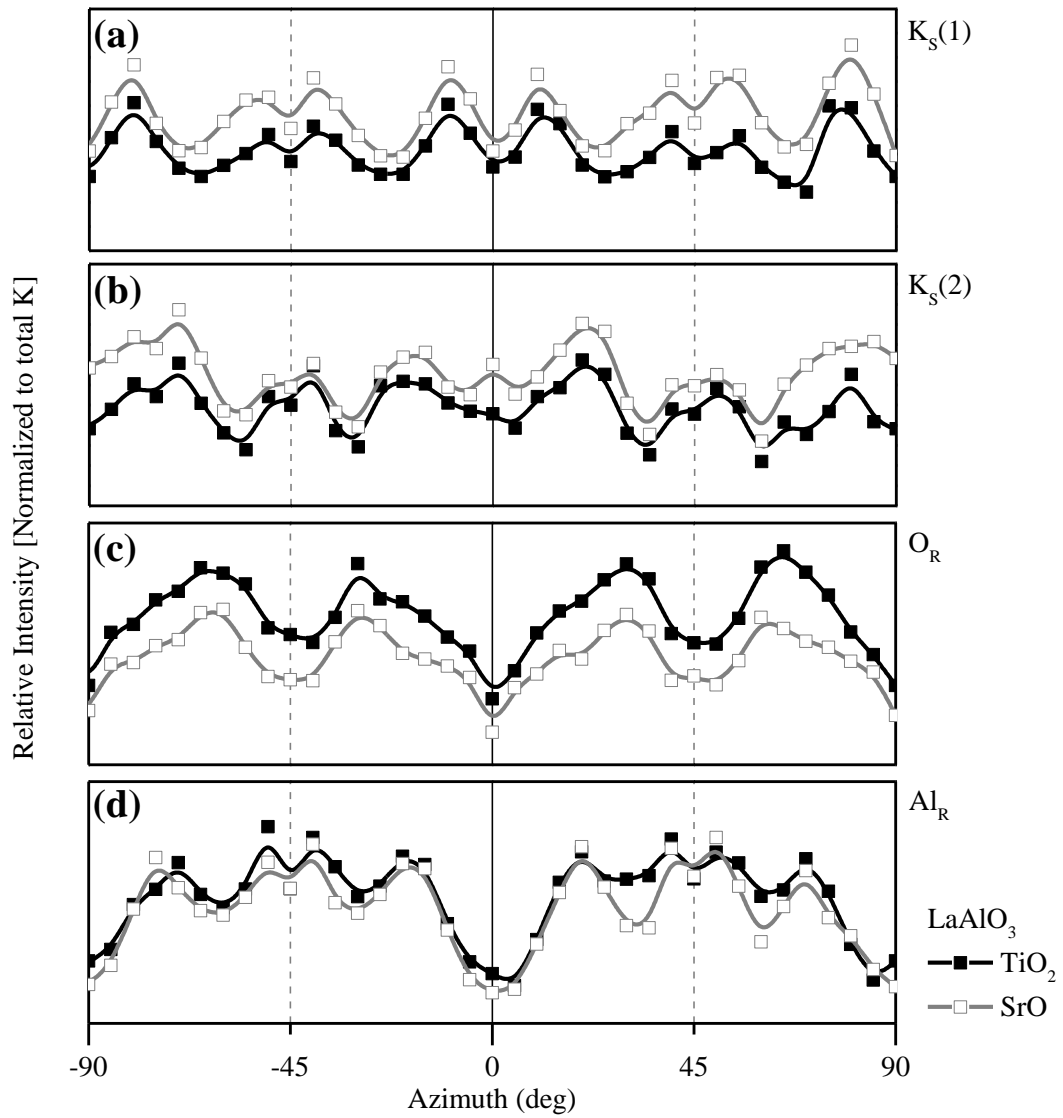
Figure 25. The normalized relative intensity values of $K_S(1)$ (a), $K_S(2)$ (b), $O_R$ (c) and $Al_R$ (d) as a function of the azimuthal angle, with filled black squares for LaAlO$_3$ on TiO$_2$-SrTiO$_3$ and empty grey squares for LaAlO$_3$ on SrO-SrTiO$_3$.

### 3.3.3 SIMULATIONS

Using the SARIC software recoil spectra were simulated for La, Al and O, for different variations of the $AlO_2$ surface. Extra LaO and $AlO_2$ layers were added using the lattice parameters for fully strained $LaAlO_3$. These spectra, along with the measured data, are plotted in Figure 26. Characteristic features that are identified in the AR-MSRI data are the minima at 0 and 45 degree, two strong peaks for Al (~20° and ~70°) and for La (~25° and ~65°), and the presence shoulders on one side of each peak. The shoulders for Al are on the 45° side of the peak and for La on the 0° and 90° sides of the peaks. The simulation for an ideal $AlO_2$ surface does not match well; at 45° there should have been a deep minimum for Al and the peaks for La are too close to 45°. An $AlO_2$ surface where 50% of the oxygen was removed (O vacancies) was only marginally different from the ideal structure. Simulating an extra layer of oxygen atoms (as claimed in [62]) shows the approximate peak positions and minima correctly, but not the shoulders. An extra layer of oxygen atoms positioned on the La sites above the $AlO_2$ layer and elevated only 0.5 Å above the $AlO_2$ plane has the closest fit for the Al spectrum, but for the La the shoulders are on the wrong side of the peaks and the peak positions are slightly off. In [appendix reference] the AR-MSRI data and simulations for O are plotted. In this case only the simulation for the vacancy model is far off and the extra layer of O atoms at La sites is the only simulated spectrum that shows the shoulders close to 45°. Although not shown in figures, simulations were ran for $AlO_2$ terminated surfaces with either elevated O or elevated Al atoms, but these adjustments did not yield better fits. Based on these simulations it is likely that there is an additional oxygen plane above the $AlO_2$ surface. However, the actual configuration could not be determined from fitting simulations to the AR-MSRI data.
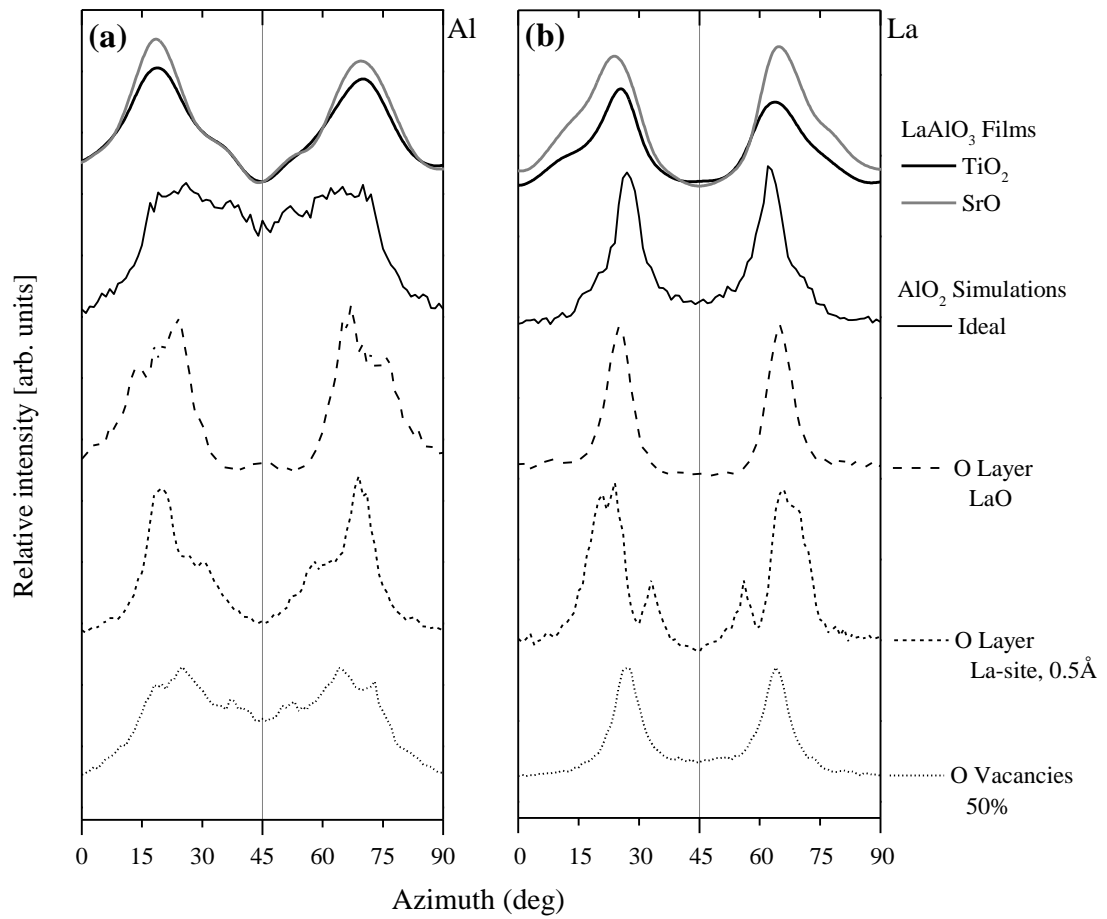
Figure 26. The relative intensities from the AR-MSRI experiments on LaAlO$_3$ grown on TiO$_2$ and SrO terminated SrTiO$_3$, with Al$^+$ in (a) and La$^+$ in (b), and the simulation results. The shown simulations are, in sequential order: the ideal AlO$_2$ terminated surface, AlO$_2$ termination with the oxygen ions from a LaO layer on top, AlO$_2$ termination with the oxygen ions at the La sites, elevated 0.5Å above the AlO$_2$ plane, and an AlO$_2$ termination where halve of the oxygen atoms is removed.

40

# 4   DISCUSSION

## 4.1   Characterization of substrate termination

AR-MSRI is used to investigate the terminating sublayer of perovskite (like) substrates that underwent treatment. Using (001) oriented $SrTiO_3$, which has a well-established singly terminated surface, as a benchmark, the method of comparing the ratio of relative intensities from the cationic species was extended. The results as presented in the previous chapter and the methods used are not without their limitations.

Substrates of (001) oriented $SrTiO_3$ have SrO and $TiO_2$ sublayers, having either of these layers at the top results in a stable surface in terms of energy. The increase in Ti at the surface after selective etching, as well as the possible reconstructions, and small deviations from the bulk crystal structure, have been extensively studied [21,39,40,69]. The result presented here is merely a confirmation and forms the foundation for the other orientations.  Experimental evidence of singly terminated $SrTiO_3$ with the (110) and (111) orientation had not yet been presented. Looking at the two available sub-layers, $SrTiO^{4+}$ and $O_2^{4-}$, alone the ability to singly terminate by Sr removal is not intuitive, as it will create vacancies in an otherwise completely occupied layer. However, the removal of a cation does reduce the positive charge on this surface layer and it will thus cause a reduction of the surface dipole. First principle calculations suggest stability of Ti rich $SrTiO_3$ (110) surfaces for Sr poor environments [43], which is the case for the selective etching as well as the annealing process. Bottin, Finocchi and Noguera suggest a model where a $TiO_2$ micro-faceted (110) surface is created as a result of charge modification effects that extend rather deeply into the surface, correlating the presence of under-coordinated atoms and the interplay between the atomic relaxations and the electron redistribution [43]. The possibility of Ti rich $SrTiO_3$ (111) surfaces has been showed by first principle calculations, which suggest that both a mixed $SrTiO_3$ (111) surface should spontaneously dissociate into SrO and $TiO_2$ rich domains [66]. Removing the SrO through selective etching would then create a $TiO_2$ terminated surface. The results presented here form a good fit with the existing body of literature and confirm experimentally that Ti rich terminations are not only stable, but can be created as well. While there are small changes in shape of (110) $SrTiO_3$ element's relative intensity spectra suggest changes in surface structure, the shapes for (001) and (111) are almost identical except for the intensity. Further investigation through a thorough analysis of the dependence of the individual relative intensities using simulations could give additional insight in the reconstructions. However, the impact of these would be limited to verification of already extensive collection of previously reported data.

Despite the popularity of $LaSrAlO_4$ as a substrate for the growth of high Tc superconductors, not surface treatments have been proposed for creating higher quality surfaces. The publication by Becerra-Toledo and Marks (2010) is the only work discussing the surface of $LaSrAlO_4$ and the effects of annealing [48]. These authors show that Sr and O segregation occurs in the form of polycrystalline islands on the (100) surfaces and claim that this system is fundamentally different from other comparable

oxides. The results of this AR-MSRI and DRS study show not only a very high similarity to comparable $LaAlO_3$ and $SrTiO_3$ in terms of relative intensities and azimuthal spectra, but show that this material can be singly terminated as well. The analysis of AR-MSRI data for a material in which four different elements are shadowing and blocking each other is complex. The surface termination hypothesized based on the AR-MSRI data was confirmed by the DRS data. It is beyond the scope of this thesis to go into the treatment methods and the AFM studies that show terraces, these will be discussed elsewhere [49]. The results are intriguing, Even though La is present in both annealing environments the substrate surface becomes La poor during the annealing procedure. The ability to singly terminate a surface with two different cationic arrangements without depositing a top layer is unsurpassed. The difference between the two observed terminations is striking, SrO is neutral and $AlO_2$ is a polar surface. While the argument of charge neutrality can be used to explain the absence of La in the SrO top layer, it cannot be applied to the $AlO_2$ layer. Further investigation of these surfaces is required to determine possible crystalline and electronic reconstructions. The analysis of the angular dependence of the relative intensities is an option, but the differences for Sr and Al are minimal.

Using the changes in the ratio between cations along the low index crystalline direction is a straightforward and intuitive way of characterizing. It has now been applied to three singly terminated classes of oxide substrates, $SrTiO_3$ with neutral sub-layers, the perovskite like $LaSrAlO_4$ and $REScO_3$ with polar sub-layers [37]. Although it is tempting to compare the peak values of the ratios to compare different materials it is meaningless without in-depth knowledge of both materials. The ion yield and neutralization rate varies strongly between individual elements and it is very sensitive to the chemical environment of the particular elements [67]. The values of the cationic ratio can only be compared for samples of the same material. When comparing different materials one can only address the shape of the ratio's angular dependence. Another variation between samples that hasn't been explored for its impact on ion yield is surface roughness. A more detailed study is necessary to make the interpretation of the cationic ratio more universal.

## 4.2   Film composition and stoichiometry

For the analysis of composition and stoichiometry of thin films grown by PLD MSRI was employed. In order to grow $Cu_2O$ thin films cheaply the abundant mineral malachite was chosen. The MSRI data for malachite featured mainly its core components copper, carbon and oxygen, other elements found in the mineral, with a much lower relative intensity, are fluorine, sodium, magnesium, aluminum, silicon, phosphorus, sulfur and chlorine. Comparing the mineral with thin film grown with PLD using the mineral as the target for ablation showed that the impurity elements largely disappear from the spectrum, indicating that these do not transfer to the substrate. Since the MSRI technique is extremely sensitive, even for very small concentrations, the absence of transfer is significant. Although ion scattering is only a surface characterization technique there are several assumptions that allow the findings to be applied to the bulk as well. First, the growth temperature is relatively low, which means that there is little diffusion into the film, limiting the surface from being relatively poor in terms of impurity density.

Secondly, since the mineral sample is pretty rough the incident ions do not merely strike the surface from above, but also from the side, increasing the recoiled ratio. Although concentrations cannot be quantified, MSRI is a very powerful tool in the identification of impurities.

The AR-MSRI technique is applied to investigate cationic vacancies in thin films of $SrTiO_3$ grown under different oxygen pressures, which were predicted by first principle calculations [55]. Although AR-MSRI not optimal for bulk standard quantitative analyses a carefully designed experiment was able to provide qualitative insight in the change in stoichiometry. In order to avoid effects of roughness and differences in termination, that were observed in 40nm thick films, very thin films (3 nm) are used in the characterization of composition as a function of growth pressure. The confirmation of $V_{Sr}$ in films grown at high oxygen pressure is based on the assumption that the ion fractions are the same for films grown at high and low oxygen pressure. Even though the AR-MSRI measurements are done under the same vacuum conditions the presence of oxygen vacancies may change the ion scattering and recoil experiments. Growing $SrTiO_3$ on $LaAlO_3$, the lattice constant was found to increase for oxygen deficient films [68]. Although this will alter the shadowing and blocking effects, the relative change is smaller than the error in incident angle and will not be significant. The same study found that the Ti valance state changes for 4-6% of the atoms when changing the growth pressure while the Sr valance is constant. This change is not expected to be of much impact to the fraction of $Ti^+$. However, verifying the stability of ion fractions would considerably improve the robustness of this study. This could, for example, be done by extending these experiments to include detectors that detect all species, such as a line-of-sight detector. It is always challenging to characterize small variations in a material's composition directly by mass spectroscopy, whether it is MSRI, SIMS or RBS, or electron spectroscopy such as x-ray photoelectron spectroscopy (XPS) or energy-dispersive x-ray spectroscopy (EDS). Using TOF-ISARS as a method of approximating bulk composition presents the observed a very sensitive technique, even very small concentrations will be picked up easily. However, concentration differences cannot be quantified, and identification is possible using comparative analysis.

## 4.3   Surfaces of grown films

The analysis of $SrTiO_3$ films grown on $SrTiO_3$ showing the change of termination through depositing a single layer of $SrRuO_3$ as a mechanism to get SrO as the topmost layer. The AR-MSRI experiment shows a large decrease in value for the $Ti^+/Sr^+$ ratio at 45° and a small change in shape that is very similar to the local minimum observed in SrO terminated $LaSrAlO_4$. The $K_S$ signals from the DRS, associated with Ti and O, are fundamentally different for the two terminations; in fact the shapes are almost each other's inverse along the low index crystalline directions. The signal of recoiled oxygen features clear differences in the low index crystalline directions for the two terminations. The angular spectrum for recoiled hydrogen, which is assumed to be coming from water, has a high intensity and strong angular dependence in case of the SrO surface. Density functional theory calculations confirm that water adsorption on the SrO surface is more

favorable than $TiO_2$ surface [69]. While the singly terminated surfaces of substrates have been studied experimentally extensively, the continuance of the termination and effectiveness of changing it with the (layer-by-layer) growth of $SrTiO_3$ thin films for buffer layers is only assumed. The results presented here provide experimental evidence of the two terminations for grown films.

$LaAlO_3$ films were grown on the $SrTiO_3$ films with two terminations. During the growth 5 clear RHEED oscillations were observed for both systems. The $Al^+/La^+$ ratio from the AR-MSRI data shows the same values for films grown on different $SrTiO_3$ terminations at 45°, corresponding to the [110] direction, indicating the same termination for the $LaAlO_3$ films despite the different bottom layers. There are, however, different values at 0°, along the [010] direction, possibly due to off stoichiometry or different surface reconstructions. The simulated spectra for an ideal $AlO_2$ surface do not match the experimental intensities for recoiled Al and La. Extra oxygen on top of the surface improve the fits, but don't yield the finer details of the AR-MSRI relative intensities. The DRS shows the same shape for both recoiled oxygen and recoiled aluminum. The angular dependence spectra for the recoiled oxygen are different from the two angular dependent recoil spectra of oxygen in $SrTiO_3$, but they share the minima along the low index crystalline directions that are characteristic for the $TiO_2$ terminated $SrTiO_3$. The $K_S$ spectra for both La and Al have the same shape for both films; the La signal is similar to Sr in $SrTiO_3$, and the Al signal shares characteristics with Ti in $SrTiO_3$. The preference for $AlO_2$ termination is consistent with the claims of Francis, Moss and Jocobson (2001) that substrate surfaces are terminated by aluminum, determined by x-ray truncation rod analysis [59]. However, simulations of the claimed relaxation of the surface oxygen atoms away from the surface and a small relaxation of the aluminum atoms into the surface did not match with the measured relative intensities. The result presented here is also in discrepancy with the works studying substrates of Kawanowa et al. (2002) who claim that both layers are stable based on low energy neutral scattering spectroscopy and with Jacobs, Miguel and Alvarez (1997) who claimed LaO was the more stable termination based on molecular dynamics [60,61]. The LaO layer seems to be unstable and what happens to the La species has to be investigated. Because of the low diffusion barriers there can be long diffusion lengths during and after the deposition [64]. A terminating LaO layer without La was suggested by a TEM study [62]. In this case all the La would have desorbed from the surface either immediately after the deposition or during the cooling down process. The relative intensity for La around 0° is significantly larger for the film grown on SrO, indicating there is still some La present at the surface. A recent first principle study showed that even for a $LaAlO_3$ film of five layers La surface vacancies are introduced for charge compensation [70]. Future investigations should include a high temperature comparison for these $LaAlO_3$ films, especially in the light of the work by Yoa et al. (1998) showing temperature dependent stability by ion scattering techniques [58].

In both the $LaAlO_3$ and $SrTiO_3$ cases the cationic ratio from the AR-MSRI data features a peak at 0°, along [010] direction, of which the origin remains to be determined since the B-site cannot be shadowing the A-site in that direction. The relative intensities

for individual elements have deep minima in this direction and the differences between substrates and grown films are hard to identify. Perhaps oxygen reconstructions, which are more likely to be created during growth than during annealing, are responsible. The potassium scattering signals from the DRS are very sensitive in terms of angular dependence as a function of termination, as can be seen from the $SrTiO_3$ data. The recoiling spectra confirm the sensitivity of hydrogen and show the use for identifying surfaces that are sensitive to adsorbed water. The recoiled oxygen has a clear angular dependence as well and can be used to distinguish two different terminations. The simulations, on the other hand, have proven to be very sensitive to small variations and the large number of variables makes AR-MSRI simulations less useful. Future work may focus on the simulation of DRS signals.

## 4.4   Techniques

A limitation in the application of TOF-ISARS to the identification of crystalline distortions is the low accuracy of the azimuthal rotation, which is limited to $5°\pm1°$. This limits the analysis of fine features that scattering and recoil spectra could show when they undergo surface reconstructions or distortions. A related drawback of this study is that the same angle of incidence was used for all studies. Although this grazing incidence is generally very effective in creating shadowing and blocking effects among the different atoms in the surface layer(s), it may not be the optimal angle. The crystalline unit cell, lattice sites and the atomic positions are different for various materials and $15°$ may not be the angle where the shadowing cone of the surface cations fully captures the cations in the second layer.

Interpreting the cationic ratios from the AR-MSRI experiments has been employed to compare the surface termination qualitatively. Signals from two separate experiments have to be compared to estimate the improvements in the single termination of the surface and one cannot quantify the coverage of the surface by the dominating terminating sub-layer. Since only ion fractions are measured it is impossible to give a theoretical value for the maximum value for the cationic ratio, which also varies with the material and nature of the surface layer. Combination of these techniques with AFM is essential, so as to one has to show that the surface is smooth and without particles or segregated phases. Comparing the shape of individual species is still challenging and perovskite cations that occupy either sites (A or B site) have peaks at the approximately the same position regardless of the composition and dimensions. Comparison with simulations suggests that the shape is mainly determined by the oxygen configuration at the surface. One should keep in mind that the validity of the simulations has yet to be verified. Although not varied in this study it is important to consider temperature changes. High ion fractions are obtained at low temperatures (where 150 °C is relatively low in regard to the growth and melting temperatures of oxides), and the ion fractions between elements may be different at higher temperatures [19]. High temperature experiments will thus yield different ratios between elements and be subject to lower signal to noise ratio due to less ions. Focusing on the identification of individual species it is important that ions with a double charge will appear as when they would have

45

approximately halve their mass, for this reason some impurities hard to determine due to the double charged peaks such as $N^+$ in the presence of $Al^{2+}$. For elements that are most commonly found with a negative charge, such as oxygen, it is counter intuitive to include the positively charged species in one's AR-MSRI characterization. However, there is always a fraction with a positive charge that can be used in the analysis. Taking oxygen as an example, the ratio is small and strongly dependent on its chemical environment, due to low yield for the production of $O^+$, but definitely present [2]. A model was created to generate analytical expressions for the positive, neutral, and negative recoil yields, from differently charged bonding environments in terms of the probabilities for ionization, excitation, and neutralization [67]. Switching the polarity of the electrodes in the reflection MSRI detector has never been used in this setup.

The use of scattered and recoiled signals from the DRS detector is a good verification method since it detects positive, neutral and negative species. The integrated signal for the total scattered potassium from the DRS experiments has a smaller increase over time and a stronger angular dependence. In the process of normalization of the DRS signals for both the recoiled species as well as the $K_S$ peaks information may be lost and angular variations of the normalized curves may be altered. Although this makes the DRS analysis less robust, the integrated signal always has peaks in the low index crystalline directions, both at 0° and 45°. This means if one sample shows a peak and another sample has a minimum, the shape is a result from the interactions at the sample. If, however, both samples have minima this could be a normalization effect. Another limitation of this study is that only easily observable peaks have been identified, theoretical predictions of the locations of other peaks have not been used.

Earlier studies using TOF-ISARS techniques, introduced in paragraph 1.3, were strongly based on simulations, whereas the results presented in this work depend mostly on comparison between two samples and the presence of minima or maxima in the low index crystalline directions. Simulations employed to support the experiments described in this thesis have not matched the experimental data as well as it did for other studies. The great similarity among different elements and different terminations indicates a limited role for simulated spectra as well. The poor match could be related to the complexity and the amount of variables that have to be taken into account for reconstructions, elevation of particular species, vacancies and extra planes, and their combinations in ternary oxides.

# 5   CONCLUSION

## 5.1   Conclusions

In this thesis the capability of analyzing the topmost atomic layers of TOF-ISARS, combining AR-MSRI and DRS, is employed to study different elements in the research of oxide systems, which are currently experiencing a strong increase in interest. Experimental evidence for a broader collection of singly terminated substrates and their orientations is presented, paving the way for studies in new directions. Further insight into elemental transfer by pulsed laser deposition (PLD) is provided by analyzing the transfer of impurity species and cationic stoichiometry. The control over the atomic layer terminating grown films is analyzed, verifying the well-defined $SrTiO_3$ surfaces and showing the termination preference for $LaAlO_3$ films.

While device design and materials research converge to smaller scales, atomic control of substrate surfaces is of great concern. In this work a complete set of experimental evidence confirms Ti rich singly terminated $SrTiO_3$ substrates in different orientations. While singly terminated substrates were already suggested in previous studies no direct evidence for Ti termination has been provided for (110) and (111) orientations. These high quality and singly terminated substrates could lead to another boost in progress of well-defined superlattice research and interface engineering. Singly terminated $LaSrAlO_4$ is presented, which can be terminated in two different ways. Next to singly terminated $SrTiO_3$ and the rare-earth scandates, which have larger in-plane lattice parameters, this marks the introduction of a singly terminated substrate available with a relatively small in-plane lattice parameter. This has important implications for studies involving termination dependent strain engineering, such as investigating the mixed phases of $BiFeO_3$ [71].

Previously the background pressure in PLD has been related to the crystal growth mode and oxygen vacancies. The suggested increase in Sr vacancies for $SrTiO_3$ films grown at high oxygen pressure in relation to films grown in high vacuum shows a more delicate dependence on background pressure for the PLD process beyond oxygen vacancies and growth mode. PLD is known for almost stoichiometric transfer of species from target to surface. The $Cu_2O$ growth from the malachite mineral shows that the evaporation at the target, transfer by plasma and atomic growth at the substrate surface can be an impurity filter. Both findings are of importance to researchers employing PLD and a temperature dependent study would be a logical next step in either case.

A striking difference between $LaAlO_3$ and $SrTiO_3$ films grown of $TiO_2$ and SrO surfaces was obtained using TOF-ISARS. Experimental evidence for two different terminations of the $SrTiO_3$ films is presented in the form of strong maxima in the Ti/Sr cationic ratio in the [110] directions, where Ti is blocking Sr for $TiO_2$ termination, and a strong decrease in the ratio with local minima in the [110] directions for SrO termination. Different angular dependencies for K scattered off Sr, Ti and O for the two cases, as well as the direct recoil spectra for O and H, leave room for no doubt about the presence of

TiO$_2$ and SrO surfaces. Identical patterns in both AR-MSRI and DRS indicate AlO$_2$ termination for LaAlO$_3$ films grown on both bottom layers. The maxima for the Al/La cationic ratio in [110] direction are the same for both structures. The shapes of the scattered K and recoiled O and Al as obtained by DRS show identical characteristics, suggesting no difference in termination. The conducting interface in the combination of LaAlO$_3$ and SrTiO$_3$ continues to attract researchers' interest. The structure is as expected for the TiO$_2$-LaO configuration, which is known for its two-dimensional electron gas (2DEG). While the polar catastrophe model has been used for explaining the creation of the 2DEG, no such model could be applied to SrO-AlO$_2$ system since the LaAlO$_3$ film is terminated with the same AlO$_2$ sub-layer. Although LaAlO$_3$ substrates have been studied by many surface sensitive techniques, most studies investigating thin films have focused on techniques probing the interface with SrTiO$_3$. With the results presented here the LaAlO$_3$-SrTiO$_3$ system may be even more complex than it is currently perceived to be. The same may be true for other systems studied for their thin film and interface properties, such as LSMO, superlattices and high T$_c$ superconductors.

Both the LaSrAlO$_4$ and the LaAlO$_3$ studies have lanthanum poor surfaces after high temperature growth and annealing. The as received LaSrAlO$_4$ substrate showed a high amount of La, while both annealing procedures at 1000 °C yield significantly lower La intensities. LaAlO$_3$ films grown at 850 °C on a SrO terminated SrTiO$_3$ surface are AlO$_2$ terminated, despite being fully strained and five full RHEED oscillations were observed. These two systems, which are different in terms of crystal structure and composition, suggest that LaO is an inherently unfavorable terminating layer. This hypothesis is supported by a recent first principle calculations study that claims $BO_2$ termination to be favored for La$BO_3$ (001), where $B$ represents various transition metals [72]. This finding could have important implications for studies employing two, presumably, different terminations of perovskites containing La.

Combining structural AR-MSRI and DRS analyses a model is created for the identification of singly terminated surfaces. Using the integrated and normalized intensities the cationic ratio of the AR-MSRI experiments, the shape and intensity of the angular dependence of the cationic ratio are compared between samples. Peaks in the low index crystalline directions suggest shadowing of elements in those directions and increases in intensity mark the dominance of one particular element. The results can be corroborated by checking the angular dependence of scattered and recoiled signals from DRS. The ion scattering community would benefit greatly from further homogeneity in their experiments. Although detectors and geometries are often different, this model is a step towards a more unified method of analysis.

## 5.2 Recommendations for further study

The AR-MSRI and DRS methods used in this study were limited to for $\alpha = 15°$. Extending the analysis to include variations in angle of incidence could be very worthwhile. Studying the scattering and recoiled species as a function of incident angle has been employed by many previous studies to determine the exact atomic positions.

Particularly the reconstructions of the polar surfaces investigated in this thesis could be described in further detail. Including angle of incidence dependent studies will, however, be an elaborate extra step to perform with the experimental setup. The incident angle measurement series should be performed at 3 different characteristic crystalline directions, 0°, 20° and 25°, and preferably a second set after a 90° rotation of the sample. Due to inaccuracy of azimuthal angle offset the exact alignment of the sample is often determined and adjusted after the measurement. In order to ensure the correct azimuthal angle the sample alignment has to be done in situ. When this study is performed with an increment of ~2.5° it will not only provide information about the atomic positions, but it will also yield to optimal shadowing angle. This could enhance the cationic ratio obtained from AR-MSRI experiments, and potentially refine the differences between samples and create sharper azimuthal dependent spectra.

Simulations using the SARIC program are another direction recommended for future studies, pursuing better fits for the AR-MSRI relative intensities as obtained by the current geometry. Simulation efforts could also be extended to find spectra fitting the DRS azimuthal dependencies for both scattered potassium and recoiled species. The experienced limitations discussed in this thesis will be challenging to overcome, but especially for the signals with different shapes for the azimuthal spectra it could pay of to invest in.

An exploration of AR-MSRI with an inversed polarity of the electrodes in the reflectron analyzer would yield an analysis of negative instead of positive ions. Particularly for systems where two different terminations have been established, such as $SrTiO_3$ and $LaSrAlO_4$, the difference between $AO$ and $BO_2$ termination of the $ABO_3$ perovskite should be apparent. The information obtained is to be used to verify the use of $O^+$ and will be a powerful way to explore the oxygen configuration and content. A closely related recommendation is to explore the data obtained from the line-of-sight (LOS) detector, which captures all the neutral atoms entering the reflectron analyzer. Together with the inverted polarity the fractions for positive, negative and neutral atoms of a particular element can be obtained, generating a 'fingerprint' characteristic for the chemical environment of the element.

Finally, it would be interesting to investigate whether the termination of $LaAlO_3$ films on SrO terminated $SrTiO_3$ surfaces is thickness dependent. Since this study shows an $AlO_2$ termination for $LaAlO_3$ films with a thickness of five unit cells, extending the experiment for 1, 2 and 10 unit cell thick films could help determine the origin of the preference for $AlO_2$ termination.

# 6 REFERENCES

[1]     Rabalais, J.W. Low energy ion beams for surface modification and film deposition. *AIP Conference Proceedings* **576**, 911-914(2001).

[2]     Hammond, M.S., Schultz, J.A. & Krauss, A.R. Surface analysis at low to ultrahigh vacuum by ion scattering and direct recoil spectroscopy. *Journal of Vacuum Science & Technology A: Vacuum, Surfaces, and Films* **13**, 1136(1995).

[3]     Cohen, D.D. et al. Ion beams for materials analysis. *Encyclopedia Physical Science &Technology* 11(2001).

[4]     Grizzi, O. et al. Time-of-flight scattering and recoiling spectrometer (TOF-SARS) for surface analysis. *Review of Scientific Instruments* **61**, 740–752(1990).

[5]     Smentkowski, V.S. et al. Novel reflectron time of flight analyzer for surface analysis using secondary ion mass spectroscopy and mass spectroscopy of recoiled ions. *Journal of Vacuum Science & Technology A: Vacuum, Surfaces, and Films* **17**, 2634(1999).

[6]     Rabalais, J.W. *Principles and Applications of Ion Scattering Spectroscopy*. (John Wiley & Sons, Inc. Hoboken, New Jersey (USA), 2003).

[7]     Ziegler, J.F., Biersack, J.P. & Littmark, U. *The Stopping and Range of Ions in Matter*. (Pergamon Press: New York (USA), 1985).

[8]     Zhang, R. et al. Application of low energy ion blocking for adsorption site determination of Na Atoms on a Cu (111) surface. *Surface Science* **604**, 1230-1236(2010).

[9]     Kim, C., Höfner, C. & Rabalais, J.W. Surface structure determination from ion scattering images. *Surface Science* **388**, L1085-L1091(1997).

[10]    Dodonov, A.I. et al. Effect of surface semichanneling on energy distributions of molecular ions reflected from single-crystal surface. *Surface Science Letters* **140**, L244–L252(1984).

[11]    Bu, H., Shi, M. & Rabalais, J.W. Surface periodicity of Ir (110) from time-of-flight and recoiling spectrometry (TOF-SARS). *Surface Science* **244**, 96-102(1991).

[12]    Auciello, O. et al. Studies of ferroelectric heterostructure thin films, interfaces, and device-related processes via in situ analytical techniques. *Integrated Ferroelectrics* **27**, 103-18(1999).

[13]    Gozar, a et al. Surface structure analysis of atomically smooth BaBiO$_3$ Films. *Physical Review B* **75**, 3-6(2007).

[14] Krauss, A.R. et al. Ion Beam Deposition and Surface Characterization of Thin Multicomponent Oxide Films During Growth. *Materials Science and Engineering A* **253**, 221-233(1998).

[15] Robinson, M.T. & Torrens, I.M. Computer simulation of atomic-displacement cascades in solids in the binary-collision approximation. *Physical Review B* **9**, 5008(1974).

[16] Niehus, H., Heiland, W. & Taglauer, E. Low-energy ion scattering at surfaces. *Surface Science Reports* **17**, 213-303(1993).

[17] Bykov, V. et al. Scattering and recoiling imaging code (SARIC). *Nuclear Instruments and Methods in Physics Research B* **114**, 371-378(1996).

[18] Herman, G.S, Sievers, M.R. & Gao, Y. Structure determination of the two-domain (1x4) anatase $TiO_2$ (001) surface. *Physical review letters* **84**, 3354-7(2000).

[19] Herman, G.S. Surface structure determination of $CeO_2$ (001) by angle-resolved mass spectroscopy of recoiled ions. *Physical Review B* **59**, 14899-14902(1999).

[20] Herman, G.S. et al. Mass spectroscopy of recoiled ions, secondary ion mass spectroscopy, and Auger electron spectroscopy investigation of $Y_2O_3$-stabilized $ZrO_2$ (100) and (110). *Journal of Vacuum Science and Technology-Section A-Vacuum Surfaces and Films* **17**, 939–944(1999).

[21] Heide, P.A.W. van der et al. X-ray photoelectron spectroscopic and ion scattering study of the $SrTiO_3$ (001) surface. *Surface Science* **473**, 59-70(2001).

[22] Mueller, A.H. et al. Real-time observations of interface formation for barium strontium titanate films on silicon. *Applied Physics Letters* **80**, 3796(2002).

[23] Taferner, W. et al. The investigation of GaN growth on silicon and sapphire using in-situ time-of-flight low energy ion scattering and RHEED. *Journal of Crystal Growth* **164**, 167-174(1996).

[24] Smentkowski, V.S. et al. Use of reactive ion sputtering to produce clean germanium surfaces in a carbon rich environment—an ion scattering study. *Journal of Vacuum Science & Technology A: Vacuum, Surfaces, and Films* **16**, 1779(1998).

[25] Bednorz, J.G. & Müller, K.A. Possible high Tc superconductivity in the Ba- La- Cu- O system. *Zeitschrift für Physik B Condensed Matter* **64**, 189–193(1986).

[26] Park, J.-H. et al. Direct evidence for a half-metallic ferromagnet. *Nature* **392**, 794–796(1998).

[27] Merz, W.J. The Electric and Optical Behavior of $BaTiO_3$ Single-Domain Crystals. *Physical Review* **76**, 1221(1949).

[28] Rijnders, G. & Blank, D.H.A. Build your own superlattice. *Nature* **433**, 369-370(2005).

[29] Ohtomo, A. & Hwang, H.Y. A high-mobility electron gas at the $LaAlO_3/SrTiO_3$ heterointerface. *Nature* **427**, 423-6(2004).

[30] Lee, H.N. et al. Strong polarization enhancement in asymmetric three-component ferroelectric superlattices. *Nature* **433**, 395–399(2005).

[31] Ueda, K., Tabata, H. & Kawai, T. Ferromagnetism in $LaFeO_3$-$LaCrO_3$ Superlattices. *Science* **280**, 1064-1066(1998).

[32] Norton, D.P. et al. Superconductivity in $SrCuO_2$-$BaCuO_2$ Superlattices: Formation of Artificially Layered Superconducting Materials. *Science* **265**, 2074-2077(1994).

[33] Bogorin, D.F. et al. Nanoscale rectification at the $LaAlO_3/SrTiO_3$ interface. *Applied Physics Letters* **97**, 013102(2010).

[34] Cen, C. et al. Oxide nanoelectronics on demand. *Science* **323**, 1026-30(2009).

[35] Yu, C. et al. Thermal conductivity reduction in oxygen-deficient strontium titanates. *Applied Physics Letters* **92**, 191911(2008).

[36] Chung, S., Yoon, D.Y. & Kang, S.-J.L. Effects of donor concentration and oxygen partial pressure on interface morphology and grain growth behavior in $SrTiO_3$. *Acta Materialia* **50**, 3361-3371 (2002).

[37] Kleibeuker, J.E. et al. Atomically Defined Rare-Earth Scandate Crystal Surfaces. *Advanced Functional Materials* **20**, 3490–3496(2010).

[38] Ngai, J.H. et al. Achieving A-Site Termination on $La_{0.18}Sr_{0.82}Al_{0.59}Ta_{0.41}O_3$ Substrates. *Advanced Materials* **22**, 2945-2948(2010).

[39] Kawasaki, M. et al. Atomic control of the $SrTiO_3$ crystal surface. *Science* **266**, 1540(1994).

[40] Koster, G. et al. Quasi-ideal strontium titanate crystal surfaces through formation of strontium hydroxide. *Applied Physics Letters* **73**, 2920(1998).

[41] Mukunoki, Y. et al. Atomically flat (110) $SrTiO_3$ and heteroepitaxy. *Applied Physics Letters* **86**, 171908(2005).

[42] Chang, J., Park, Y.-S. & Kim, S.-K. Atomically flat single-terminated SrTiO$_3$ (111) surface. *Applied Physics Letters* **92**, 152910(2008).

[43] Bottin, F., Finocchi, F. & Noguera, C. Stability and electronic structure of the (1×1) SrTiO$_3$(110) polar surfaces by first-principles calculations. *Physical Review B* **68**, 035418(2003).

[44] Chang, J., Park, Y.-S. & Kim, S.-K. Atomically flat single-terminated SrTiO$_3$ (111) surface. *Applied Physics Letters* **92**, 152910(2008).

[45] Biswas, A. et al. Universal Ti-rich termination of atomically flat SrTiO$_3$ (001), (110), and (111) Surfaces. *Applied Physics Letters* **98**, 051904(2011).

[46] Brown, R. et al. Low-loss substrate for microwave application of high-temperature superconductor films. *Applied Physics Letters* **57**, 1351(1990).

[47] Zvereva, I., Zueva, L. & Choisnet, J. Metastability of the K$_2$NiF$_4$ type structure of the solid solution LaCa(Cr$_x$Al$_{1-x}$)O$_4$ (0<<x<<0.10). *Journal of Materials Science* **30**, 3598-3602(1995).

[48] Becerra-Toledo, A E. & Marks, L.D. Strontium oxide segregation at SrLaAlO$_4$ surfaces. *Surface Science* **604**, 1476-1480(2010).

[49] Rossen, P.B. et al. Singly terminating LaSrAlO$_4$ surfaces A-site or B-site using a cation rich annealing process. In preparation.

[50] Davenport, W.G.I. et al. *Extractive metallurgy of copper*. (Pergamon Press, Oxford (England), 2002).

[51] Balasubramaniam, K.R. et al. Semiconductor thin films directly from minerals - Study of structural, optical, and transport characteristics of Cu$_2$O thin films from malachite mineral and synthetic CuO. *Thin Solid Films - Accepted* (2011).

[52] Ohnishi, T. et al. Defects and transport in complex oxide thin films. *Journal of Applied Physics* **103**, 103703(2008).

[53] Keeble, D. et al. Identification of A- and B-Site Cation Vacancy Defects in Perovskite Oxide Thin Films. *Physical Review Letters* **105**, 3-6(2010).

[54] Shanthi, N. & Sarma, D. Electronic structure of electron doped SrTiO$_3$: SrTiO$_{3-\delta}$ and Sr$_{1-x}$La$_x$TiO3. *Physical Review B* **57**, 2153-2158(1998).

[55] Erketin et al. Interplay between Intrinsic Defects, Doping, and Free Carrier Concentration in Perovskite Oxide Thin Films. Under Review.

[56] Thiel, S. et al. Tunable quasi-two-dimensional electron gases in oxide heterostructures. *Science* **313**, 1942-5(2006).

[57]    Huijben, M. et al. Structure-Property Relation of $SrTiO_3$/$LaAlO_3$ Interfaces. *Advanced Materials* **21**, 1665-1677(2009).

[58]    Yao, J. et al. Thermal stimulation of the surface termination of $LaAlO_3${100}. *The Journal of Chemical Physics* **108**, 1645(1998).

[59]    Francis, R., Moss, S. & Jacobson, A. X-ray truncation rod analysis of the reversible temperature-dependent [001] surface structure of $LaAlO_3$. *Physical Review B* **64**, 235425(2001).

[60]    Kawanowa, H. et al. Structure analysis of $LaAlO_3$ (001) surfaces by low energy neutral scattering spectroscopy. *Surface Science* **506**, 87-92(2002).

[61]    Jacobs, J.-P., Miguel, M.A.S. & Alvarez, L.J. Studies of $LaAlO_3$ (100) surfaces by molecular dynamics simulations. *Journal of Molecular Structure (Theochem)* **390**, 193–198(1997).

[62]    Lanier, C. et al. Surface Reconstruction with a Fractional Hole: ($\sqrt{5}\times\sqrt{5}$)R26.6° $LaAlO_3$ (001). *Physical Review Letters* **98**, 98-101(2007).

[63]    Qiao, L. et al. Thermodynamic instability at the stoichiometric $LaAlO_3$/$SrTiO_3$(001) interface. *Journal of physics. Condensed matter* **22**, 312201(2010).

[64]    Ferguson, J.D., Kim, Y. & Woll, A.R. Thickness dependence of surface diffusion in epitaxial $LaAlO_3$ on $SrTiO_3$ (001). *Arxiv preprint arXiv:1010.5548* **2**, 1-4(2010).

[65]    Rijnders, G. et al. Enhanced surface diffusion through termination conversion during epitaxial $SrRuO_3$ growth. *Applied Physics Letters* **84**, 505(2004).

[66]    Marks, L.D. et al. The small unit cell reconstructions of $SrTiO_3$ (111). *Surface Science* **603**, 2179-2187(2009).

[67]    Chen, J.N. & Rabalais, J.W. Effects of chemical environment on direct recoil ion fractions. *Journal of the American Chemical Society* **110**, 46–52(1988).

[68]    Cai, H.L., Wu, X.S. & Gao, J. Effect of oxygen content on structural and transport properties in $SrTiO_{3-x}$ thin films. *Chemical Physics Letters* **467**, 313-317(2009).

[69]    Evarestov, R., Bandura, A. & Alexandrov, V. Adsorption of water on (001) surface of $SrTiO_3$ and $SrZrO_3$ cubic perovskites: Hybrid HF-DFT LCAO calculations. *Surface Science* **601**, 1844-1856(2007).

[70]    Seo, H. & Demkov, A. First-principles study of polar LaAlO (001) surface stabilization by point defects. *Physical Review B* **84**, 1-9(2011).

[71]    Zeches, R.J. et al. A strain-driven morphotropic phase boundary in BiFeO3. *Science* **326**, 977-80(2009).

[72]    Lee, Y.-L. et al. Ab initio energetics of La*B*O$_3$(001) (B = Mn , Fe, Co, and Ni) for solid oxide fuel cell cathodes. *Physical Review B* **80**, (2009).

# 7 APPENDICES
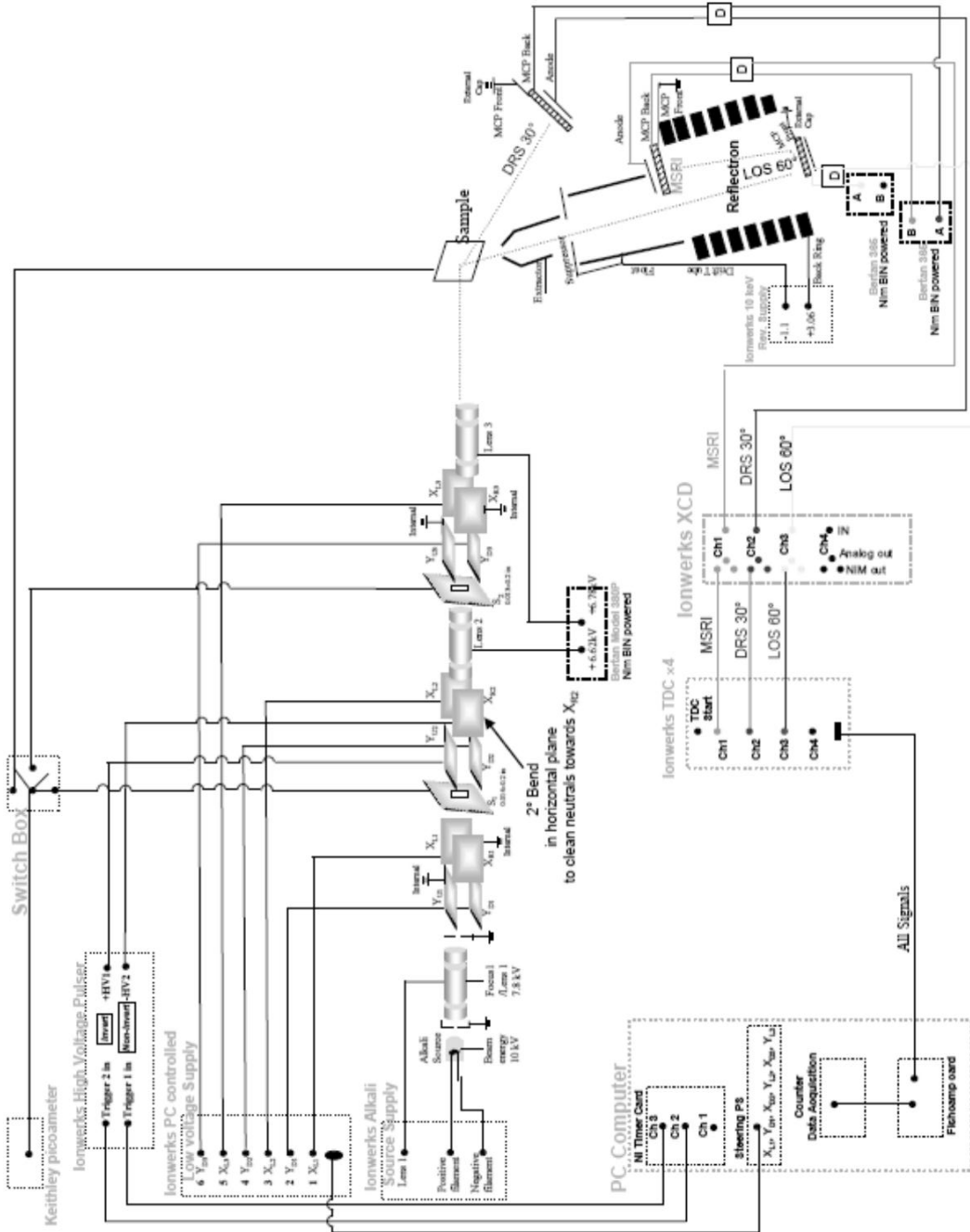
## 7.1 TOF-ISARS electronics and mechanical hardware

Figure 27. Schematic of TOF-ISARS electronics and mechanical hardware.

## 7.2 MATLAB Analysis script LaAlO₃

**%% Set parameters for analysis**
Name = 'film_date_tilt15-'

%MSRI
%Element 1: K
Mass1_a= 37.5;     %estimated start of peak (AMU)
Mass1_b= 43;       %estimated end of peak (AMU)
%Element 2: Al
Mass2_a= 25.0;     %estimated start of peak (AMU)
Mass2_b= 30.5;     %estimated end of peak (AMU)
%Element 3: La
Mass3_a= 130;      %estimated start of peak (AMU)
Mass3_b= 150;      %estimated end of peak (AMU)
%Element 4: O
Mass4_a= 14;       %estimated start of peak (AMU)
Mass4_b= 17;       %estimated end of peak (AMU)

%DRS
%Peak positions
Peak1=505;
Peak2=531;
Peak3=548;
Peak4=563;
Peak5=567;

%Angle correction
Correction = 360;     %the standard bias included in our system is 5 degrees

**%% Definition of files that should be imported**
file_nr = 41;      %Number of measurements (ie # datafiles)
Angle_start = 260;  %Angle of first measurement
Angle_end = 460;    %Angle of last measurement
Angle_spacing = 5;  %Spacing between measured angels

file001 = [Name 'azi260.txt'];
…
file041 = [Name 'azi460.txt'];

n=1700-250;      %Number of datapoints that
filearray = [file001;…;file041];

## %% Analysis Script MSRI

```
Angle = [Angle_start:Angle_spacing:Angle_end];
Angle_corrected = Angle(:) – Correction;

Count_norm_1 = zeros(file_nr,1) ;
…
Count_norm_5 = zeros(file_nr,1) ;

for file_index=1:file_nr
   file=filearray(file_index,:);

     %Peak element 1
     X_1 = dlmread(file, '\t', 'A250..A1700');
     Y_1 = dlmread(file, '\t', 'B250..B1700');
     Count_1=0;
     for index=1:n
       if (X_1(index) < Mass1_a)
          Y_1(index) = 0;
       elseif (X_1(index)> Mass1_b)
          Y_1(index) = 0;
        end
     Count_1=Count_1+Y_1(index);
     end

     %Peak element 2
                 …
     %Peak element 3
                 …
     %Peak element 4
                 …
     %Peak element 5
                 …
   time = dlmread(file, '\t', 'B1..B10');
   Count_norm_1(file_index) = Count_1/time(8);
   Count_norm_2(file_index) = Count_2/time(8);
   Count_norm_3(file_index) = Count_3/time(8);
   Count_norm_4(file_index) = Count_4/time(8);
   Count_norm_5(file_index) = Count_5/time(8);
end

Ratio_norm1 = Count_norm_2./Count_norm_5;
…
Ratio_norm5 = Count_norm_5./Count_norm_1;
```

## %% Analysis Script DRS

```
Value_list_1 = zeros(file_nr,1) ;
…
Value_list_5 = zeros(file_nr,1) ;
Value_list_K = zeros(file_nr,1) ;

for file_index=1:file_nr
  file=filearray(file_index,:);
  values = dlmread(file, '\t', 'C10..C1000');
  Value_list_1(file_index) = values(Peak1)/time(8);
        …
  Value_list_5(file_index) = values(Peak5)/time(8);


    k=991;
    X_K = [1:1:k];
    Y_K = dlmread(file, '\t', 'C10..C1000');
    Count_K=0;
    for index=1:k
      if (X_K(index) < 556)
        Y_K(index) = 0;
      elseif (X_K(index)> 630)
        Y_K(index) = 0;
      end
    Count_K=Count_K+Y_K(index);
    end


  Value_list_K(file_index) = Count_K/time(8);

end

Ratio_DRS_1 = Value_list_1./Value_list_K;
…
Ratio_DRS_5 = Value_list_5./Value_list_K;
```


## %% Export

```
MatrixMSRI = [Angle_corrected, Count_norm_1, Count_norm_2, Count_norm_3,
Count_norm_4,Count_norm_5, Count_norm_6,Ratio_norm, Ratio_norm2, Ratio_norm3,
Ratio_norm4,Ratio_norm5, Ratio_norm6];
exportnameMSRI = ['MSRI_ analysis_' Name '.txt'];
dlmwrite(exportnameMSRI,MatrixMSRI,'delimiter', '\t','precision', '%.7f','newline', 'pc');

MatrixDRS = [Angle_corrected, Ratio_norm,
Ratio_DRS_1,Ratio_DRS_2,Ratio_DRS_3,Ratio_DRS_4,Ratio_DRS_5,Ratio_DRS_6,Value_list_K ];
exportnameDRS = ['DRS_ analysis_' Name '.txt'];
dlmwrite(exportnameDRS,MatrixDRS,'delimiter', '\t','precision', '%.7f','newline', 'pc');
```

## 7.3 Relative intensities from AR-MSRI on SrTiO$_3$

The Ti$^+$ and Sr$^+$ AR-MSRI signals for the treated SrTiO$_3$ substrates are presented in Figure 28 and the O$^+$ is presented in Figure 29. For both figures the (001), (110) and (111) orientations are presented in figure (a), (b) and (c) respectively. The crystal symmetry features associated with the various substrate orientations are readily observed. Note that Ti$^+$ and Sr$^+$ data is only shown for the treated substrates.
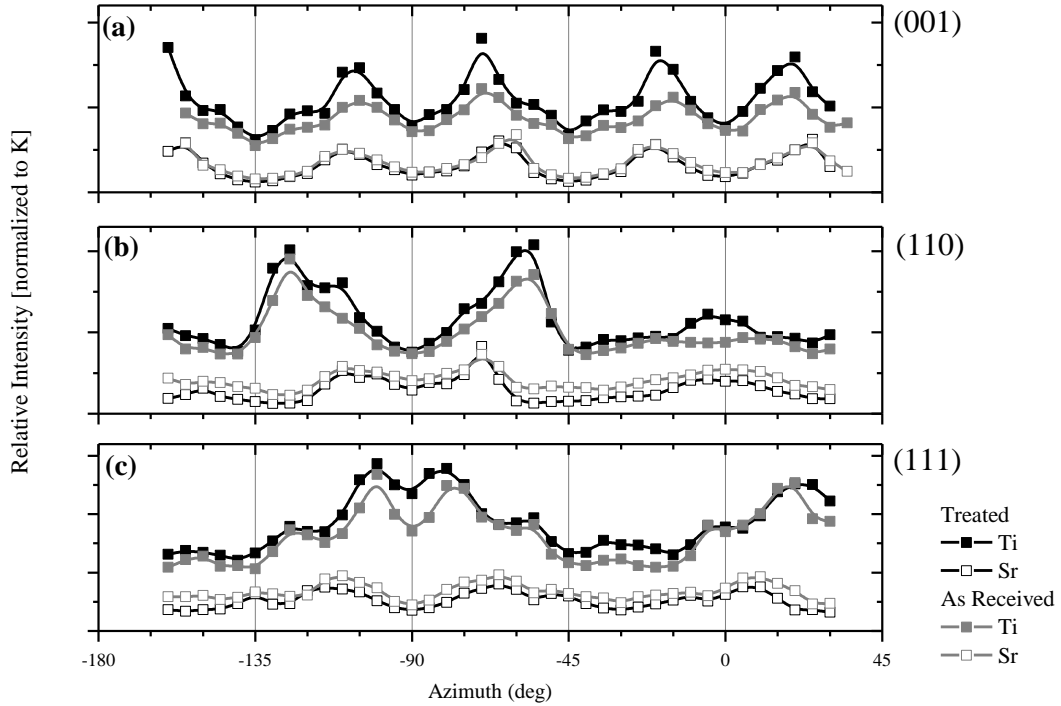


Figure 28. Relative intensities Ti$^+$ (filled) and Sr$^+$ (open) for treated (black) and as received (grey) SrTiO$_3$ substrates with orientations (001) (a), (110) (b) and (111) (c).
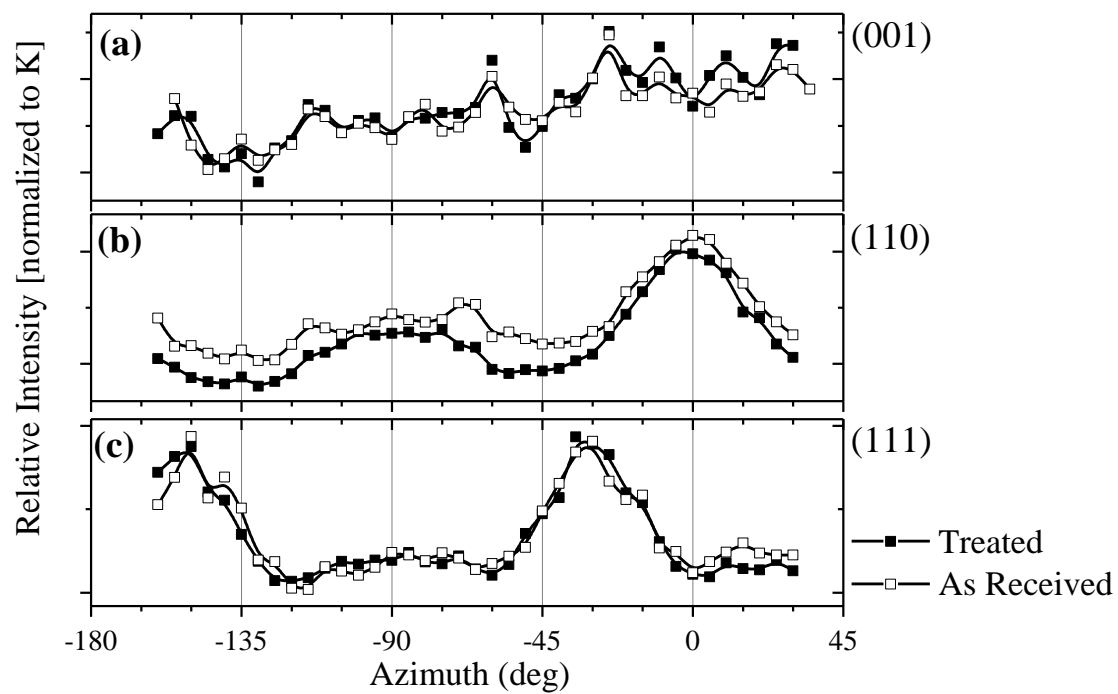
Figure 29. Relative intensities O$^+$ for treated (filled) and as received (open) SrTiO$_3$ substrates with orientations (001) (a), (110) (b) and (111) (c).

## 7.4 Relative recoil intensities from DRS on LaSrAlO₄

The relative recoil intensities of the $H_R$ and $O_R$ of as received and annealed LaSrAlO₄ substrates are shown in Figure 30. The $H_R$ is too close to the noise level to be analyzed based on overall intensity. There is a very slight modulation, peaks in the low index crystalline directions, for the La₂O₃ sample, which might be related to water adsorbed to the surface. The $O_R$ signal features some angular dependent features but the intensity of the modulation and the differences between the samples are too small for the $O_R$ signal to be analyzed.
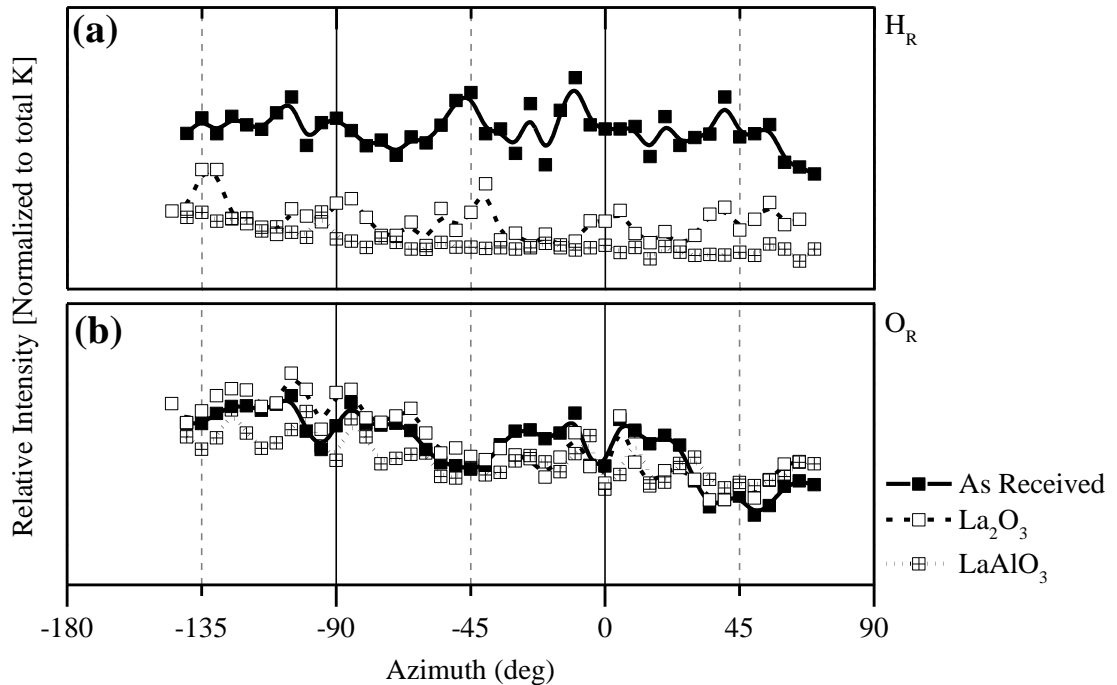


Figure 30. The normalized relative intensity values of $H_R$ (a) and $O_R$ (b) of LaSrAlO₄ as a function of the azimuthal angle, with filled squares for as received, open squares for La₂O₃ and crossed squares for LaAlO₃ annealed samples.

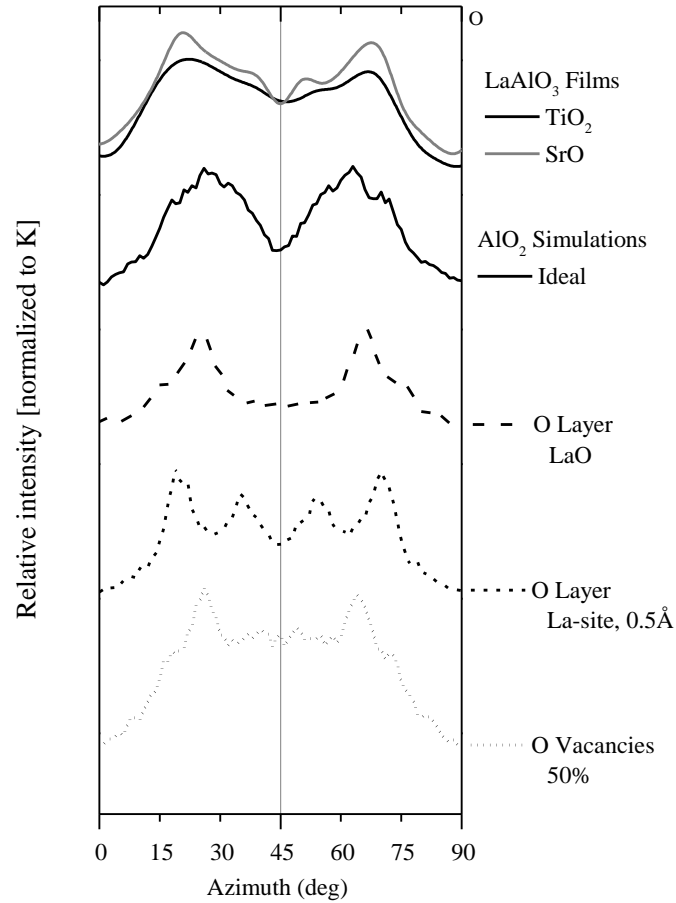## 7.5   Simulations for $O_R$ from LaAlO$_3$ films



Figure 31. Presented are the relative O$^+$ intensities from the AR-MSRI experiments on LaAlO$_3$ grown on TiO$_2$ and SrO terminated SrTiO$_3$, and the simulation results which are plotted in the same figures. The shown simulations are, in sequential order: the ideal AlO$_2$ terminated surface, AlO$_2$ termination with the oxygen ions from a LaO layer on top, AlO$_2$ termination with the oxygen ions at the La sites, elevated 0.5 Å above the AlO$_2$ plane, and an AlO$_2$ termination where halve of the oxygen atoms is removed.